Journal of Inorganic Biochemistry 201 (2019) 110809

Contents lists available at ScienceDirect

Journal of Inorganic Biochemistry

journal homepage: www.elsevier.com/locate/jinorgbio

Platinum(II) coordination compounds with 4′-pyridyl functionalized 2,2′:6′, 2″-terpyridines as an alternative to enhanced chemotherapy efficacy and reduced side-effects

Sandra Altmann[a,b], Katarzyna Choroba[c,*], Magdalena Skonieczna[d,e], Dorota Zygadło[a,b], Magdalena Raczyńska-Szajgin[a,b,f], Anna Maroń[c], Jan Grzegorz Małecki[c], Agata Szłapa-Kula[c], Mateusz Tomczyk[g], Alicja Ratuszna[a,b], Barbara Machura[c], Agnieszka Szurko[a,b,**]

[a] Silesia Center for Education and Interdisciplinary Research, 75. Pułku Piechoty 1A, 41-500 Chorzów, Poland
[b] August Chełkowski Institute of Physics, University of Silesia, 75. Pułku Piechoty 1A, 41-500 Chorzów, Poland
[c] Department of Crystallography, Institute of Chemistry, University of Silesia, Szkolna 9, 40-006 Katowice, Poland
[d] Systems Engineering Group, Silesian University of Technology, Institute of Automatic Control, Akademicka 16, 44-100 Gliwice, Poland
[e] Biotechnology Centre, Silesian University of Technology, Krzywoustego 8, 44-100 Gliwice, Poland
[f] Department of Biophysics and Morphogenesis of Plants, University of Silesia, Jagiellońska 28, 40-032 Katowice, Poland
[g] Faculty of Chemistry, Silesian University of Technology, Strzody 9, 44-100 Gliwice, Poland

ARTICLE INFO

Keywords:
Platinum(II) complexes
4′-functionalized 2,2′:6′,2″-terpyridines
DNA-binding
Cytotoxicity
Apoptosis
qRT-PCR

ABSTRACT

Two platinum(II) coordination compounds, [PtCl(4′-R^1-terpy)](SO_3CF_3) (**1**) and [PtCl(4′-R^2-terpy)](SO_3CF_3) (**2**), with 4′-(2-pyridyl)-2,2′:6′,2″-terpyridine (4′-R^1-terpy) or 4′-(3-pyridyl)-2,2′:6′,2″-terpyridine (4′-R^2-terpy) were synthesized and the impact of the pendant pyridyl ring on the structure and cytotoxic activity of Pt(II)-terpyridine complexes was explored. The single-crystal X-ray diffraction analysis confirmed square planar coordination of the cations [PtCl(4′-R^n-terpy)]$^+$. The mode of binding of **1** and **2** to calf thymus DNA was examined by UV–Vis absorption titration, ethidium displacement assay and reaction with 9-ethylguanine, and the mixed covalent-intercalative mode was demonstrated. The cytotoxicity of the Pt(II) complexes against six cancer cell lines and three normal ones was determined using MTS (3-(4,5-dimethylthiazol-2-yl)-5-(3-carboxymethoxyphenyl)-2-(4-sulfophenyl)-2H-tetrazolium) assay and compared to cisplatin. The IC_{50} values for the compound **2** towards the cancer cell lines are in the low micromolar range. Most remarkably, **2** was over 4 times more effective than **1** and cisplatin against non-small lung adenocarcinoma (A549), and its selectivity index was ~60–80 times higher than that for **1** and cisplatin. The mechanisms underlying the loss of viability under treatment of **2** was further investigated including F-actin staining, mitotic index analysis, cytometric cell cycle analysis, Fluorescein isothiocyanate (FITC) -conjugated Annexin V antibody and propidium iodide (PI) staining, measurements of reactive oxygen species (ROS) in cells, analysis of changes in the mitochondrial mass and potential and quantitative real time polymerase chain reaction (qRT-PCR) genes analysis. The compound **2** was found to have a pro-oxidative effect by strong stimulation of cells for the production of reactive oxygen species and cytostatic effect through cell cycle arrest.

1. Introduction

In the last decades, 4′-functionalized 2,2′:6′,2″-terpyridines (4′-R-terpy) have attracted widespread scientific attention owing to their photophysical and electrochemical properties as well as their coordination ability [1–12]. 2,2′:6′,2″-terpyridines, being able to coordinate to both low- and high-oxidation state metal ions in a tridentate or bidentate bonding mode, form complexes of great potential for catalysis [13–16], molecular electronics [5,12,17–21], supramolecular chemistry [18,22–25] and chemotherapy [18,26–31]. Noteworthy, the substituents (R) incorporated into the central pyridine control self-assembly processes, redox and photophysical properties of 2,2′:6′,2″-terpyridines and their transition metal complexes, as well as they induce new functionalities through further derivative reactions [23,32–35].

* Corresponding author.
** Correspondence to: A. Szurko, August Chełkowski Institute of Physics, University of Silesia, 75. Pułku Piechoty 1A, 41-500 Chorzów, Poland.
E-mail addresses: katarzyna.choroba@us.edu.pl (K. Choroba), agnieszka.szurko@us.edu.pl (A. Szurko).

https://doi.org/10.1016/j.jinorgbio.2019.110809
Received 11 June 2019; Received in revised form 22 August 2019; Accepted 24 August 2019
Available online 30 August 2019
0162-0134/

For metal-based drugs, the ligand nature is of particular importance in the binding of the complex to a biomolecule such as DNA or protein [36–41].

In our previous work, we demonstrated the possibility of tuning the antitumor behavior of the square-planar $[AuCl(4'\text{-R-terpy})](PF_6)_2$ by attaching suitable substituent to the central pyridine ring of 2,2′:6′,2″-terpyridine [42]. To control cytotoxic activity of gold(III)-terpyridine complexes, we chose 4′-(2-pyridyl)-2,2′:6′,2″-terpyridine (4′-R^1-terpy) and 4′-(3-pyridyl)-2,2′:6′,2″-terpyridine (4′-R^2-terpy). The both ligands bound to the metal center in a tridentate coordination mode leaving the pendant pyridyl ring available for further interactions. Due to the presence of pendant pyridyl nitrogen and hydrogen atoms they could act as both hydrogen-bond acceptors and donors, but formation of hydrogen bonds and architecture of supramolecular frameworks were strongly dependent on the position of the nitrogen atom in the substituent ring. The ligands differed also in the dihedral angle between the least squares planes of the 2,2′:6′,2″-terpyridine skeleton and R substituent ring. As the pendant pyridyl nitrogen moves closer to the terpy unit, the molecule 4′-R-terpy achieves a more planar geometry, which leads to the increased conjugation [43–47]. We presented that this rather subtle structural difference between 4′-R^1-terpy and 4′-R^2-terpy had significant impact on the activity of $[AuCl(4'\text{-}R^1\text{-terpy})](PF_6)_2$ and $[AuCl(4''\text{-}R^2\text{-terpy})](PF_6)_2$. While the first complex exhibited pro-apoptotic activation, the second one showed pro-necrotic activity [42].

2. Results and discussion

2.1. Synthesis and characterization of Pt(II) complexes

Continuing our investigation on transition metal coordination compounds incorporating 4′-functionalized 2,2′:6′,2″-terpyridines and taking into consideration that a metal ion plays a crucial role in determining the therapeutic properties of coordination compounds, we synthetized $[PtCl(4'\text{-}R^1\text{-terpy})](SO_3CF_3)$ (**1**) and $[PtCl(4'\text{-}R^2\text{-terpy})](SO_3CF_3)$ (**2**) in order to investigate the impact of n-pyridyl substituent on antiproliferative behavior of Pt(II) systems.

The complexes $[PtCl(4'\text{-}R^1\text{-terpy})](SO_3CF_3)$ (**1**) and $[PtCl(4'\text{-}R^2\text{-terpy})](SO_3CF_3)$ (**2**) (Fig. 1) were conveniently prepared by the modified procedure of Büchner [48], with the use of the appropriate 2,2′:6′,2″-terpyridine ligand and $[PtCl_2(NCPh)_2]$ as a metal precursor.

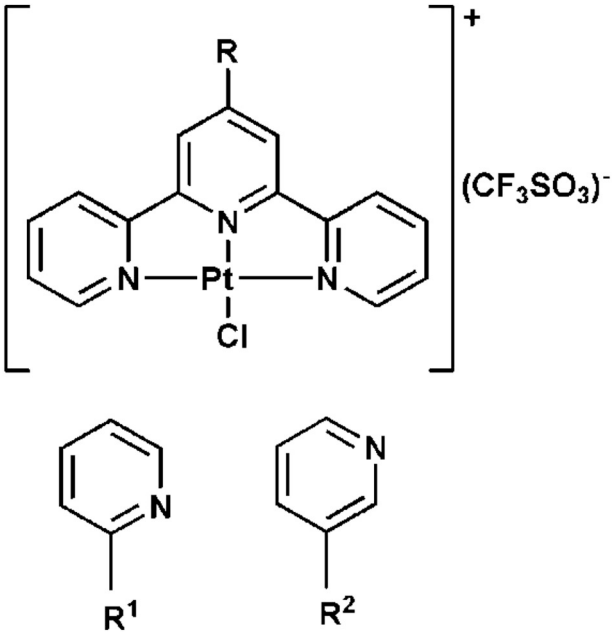

Fig. 1. Platinum(II) complexes presented in this work.

The molecular structures of **1–2** were investigated by Fourier-transformed infrared spectroscopy (FT-IR) technique (Fig. S1), high resolution mass spectroscopy with electrospray ionization (ESI-HRMS) (Fig. S2), ^1H and ^{13}C NMR spectroscopy and multidimensional NMR techniques: heteronuclear $^1H—^{13}C$ multiple bond correlation (HMBC), heteronuclear $^1H—^{13}C$ multiple quantum correlation (HMQC) and homonuclear $^1H—^1H$ correlation spectroscopy (COSY) (Figs. S3–S5) as well as they were confirmed by X-ray crystallography (Fig. 2).

The stretching vibrations assigned to $\nu_a(SO_3)$, $\nu_s(SO_3)$ and $\delta_a(SO_3)$ of the SO_3CF_3 anion occur in the IR spectra of the Pt(II) complexes at 1260, 1030 and 638 cm^{-1} [49], while characteristic bands attributed to $\nu(C=N)$, $\nu(C=C)$ stretching modes of the chelating ligand 4′-R^n-terpy are seen in the range 1607–1556 cm^{-1}. The full assignment of the signals in the ^1H and ^{13}C NMR spectra was performed on the basis of the multidimensional techniques $^1H—^{13}C$ HMBC, $^1H—^{13}C$ HMQC, $^1H—^1H$ COSY. Signals in the aromatic region of the NMR spectra are downfield shifted in relation to the free ligands, which is attributed to the impact of the complexation of platinum(II).

X-Ray analysis revealed that the compounds 1 and 2 are isomorphous, and they crystallize in the triclinic space group $P\bar{1}$. Their structures consist of $[PtCl(4'\text{-R-terpy})]^+$ cations and $SO_3CF_3^-$ packed in molar ratio 1:1, interlinked by electrostatic forces, weak hydrogen bonds and π···π and Cl···π type interactions. Perspective views showing the asymmetric units of 1 and 2 with the atom numbering are presented in Fig. 2. The selected bond lengths and angles are gathered in Table S1 in ESI.

In the cations $[PtCl(4'\text{-}R^n\text{-terpy})]^+$, the platinum atom displays a distorted square planar coordination defined by three nitrogen atoms of the 4′-substituted 2,2′;6′,2″-terpyridine ligand and chloride ligand. The angular deviation from the ideal square planar geometry, reflected by the structural parameters τ_4 ($\tau_4 = \frac{360° - (\alpha+\beta)}{360° - 2\theta}$) and τ'_4 ($\tau'_4 = \frac{\alpha-\beta}{360°-\theta} + \frac{180°-\beta}{180°-\theta}$, where α and β are the greatest valence angles, and $\beta > \alpha$) [50,51] equal 0.148 and 0.097 for **1** and 0.131 and 0.089 for **2**, can be attributed to steric requirements of 4′-R-terpy ligand and formation of two fused five-member chelate rings with the metal center. The bond angles N(1)–Pt(1)–N(2) (81.1(2)° for **1** and 81.6(3)° for **2**) and N(1)–Pt(1)–N(3) (81.1(2)° for **1** and for 81.1(3)° for **2**), are significantly smaller than 90° expected for an ideal square planar geometry. Typically for platinum(II)-terpyridine complexes of square planar geometry [52–67], the Pt—N bond of the central pyridyl ring of 4′-R-terpy ligand (Pt(1)–N(1) = 1.938(5) Å for **1** and 1.947(7) Å for **2**) is shorter than those of the outer rings (Pt(1)–N(2) = 2.010(5) Å for **1** and 2.032(8) for Å **2**; Pt(1)–N(3) = 2.014(6) Å for **1** and 2.006(8) Å for **2**). The Pt—Cl distances (2.3110(16) Å for **1** and 2.304(2) Å for **2**) are also unexceptional and they are in good agreement with those reported for the related structures [52–67].

In **1** and **2**, the 4′-subsituted 2,2′:6′,2″-terpyridine ligands are approximately planar. The dihedral angles between the inner and outer coordinated rings are 1.98° and 3.64° for **1** and 1.51° and 2.14° for **2**, while the twist angle for the substituent ring with respect to the central ring of the *terpy* framework is 3.56° for **1** and 1.33° for **2**. The molecular packing of **1** and **2** revealed a linear chain-like arrangement of the planar cations $[PtCl(4'\text{-R-terpy})]^+$, achieved through weak intermolecular hydrogen bonds C—H···Cl and C—H···N. These chains are interlinked *via* hydrogen bonds involving $SO_3CF_3^-$ anions and terpy-based ligand into layers (Fig. S6a and c), which are further assembled by Pt···Pt, π···π and Cl···π interactions (Fig. S6b and d). The interlayer metal-metal distances are 3.3821(4) [Pt(1···Pt(1)$^{(i)}$] [symmetry code: (i) = 2-x,1-y,1-z] for **1** and 3.4373(7) [Pt(1)···Pt(1)$^{(j)}$] [symmetry code: (j) = 1-x,1-y,-z] for **2**.

A summary of the intermolecular contacts in the crystal structures **1** and **2** is provided in spots of Hirshfeld surfaces [68–70] mapped with d_{norm} and in two-dimensional (2D) fingerprint plots (Fig. 3). The relative contributions of various intermolecular interactions to the Hirshfeld surfaces are illustrated in Fig. 3c, and metric parameters of

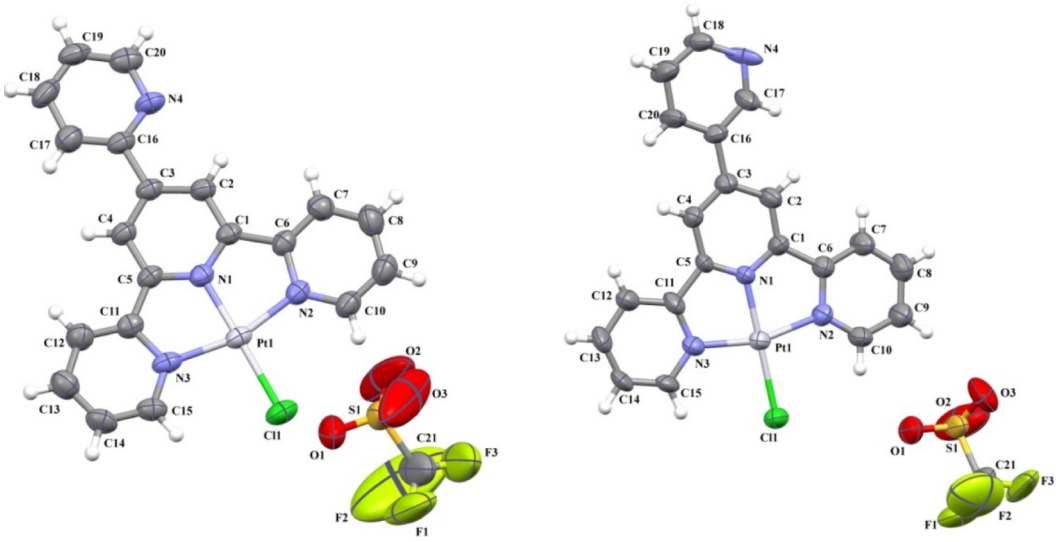

1 [PtCl(4′-R^1-terpy)](SO$_3$CF$_3$) **2 [PtCl(4′-R^2-terpy)](SO$_3$CF$_3$)**

Fig. 2. Molecular structures of **1** and **2** together with the atom numbering. Displacement ellipsoids are drawn at 50% probability level.

the intermolecular contacts are gathered in Tables S2–S5 in ESI. The striking difference between **1** and **2** concerns the participation of the H···N contacts, which are significantly larger in the case of **2**.

The cyclic voltammograms of **1** and **2** exhibit two or three reduction processes, irreversible or quasi-reversible in nature (Fig. S7 and Table S6). As the first reduction potential takes the same value (−1.37 V) for **1** and **2** and it is comparable to that of the [PtCl(terpy)]$^+$ system [59,71,72] and [PtCl(4′-R-terpy)]$^+$ system [59,71,73–77], it can be assumed that the reduction process occurs at π-deficient terpyridine core. The reduction within terpyridine fragment is anodically shifted by 0.83–0.96 V in platinum complexes compared to the free ligands [11]. The irreversible oxidation waves of **1–2** correspond to the oxidation potentials observed for the free ligands (1.20–1.44 V), and they are in higher potential region compared to that for [PtCl(terpy)]Cl (E_{ox} = 1.14 V) [78].

Both Pt(II) complexes display strong absorptions in the high energy UV-region (250–350 nm), attributable to spin allowed intraligand (IL) π → π* transitions of the terpyridyl ligand (Fig. S8 and Table S7). The lower energy bands of **1–2** are predominately contributed by metal-to-ligand charge transfer transitions (MLCT) [52,53,76,77,79–81]. Compared to [PtCl(terpy)](SO$_3$CF$_3$), this band is batochromically shifted by 38 nm for **1** and 9 nm for **2**. Replacement of 4′-(2-pirydyl)-2,2′:6′,2″-terpyridine (in **1**) by 4′-(3-pirydyl)-2,2′:6′,2″-terpyridine (in **2**) leads to shift of MLCT absorption band towards higher energy (from 432 nm in **1** to 403 nm in **2**), reflecting larger withdrawing effect of 2-pirydyl substituent compared to that of 3-pirydyl one [82,83]. In higher concentrations (250–500 μM), the lowest energy band of **1** and **2** does not obey the Beer–Lambert's law (Fig. S9a), signaling aggregation processes of the Pt(II) complexes through π-π interaction of terpyridine ligands, which is also supported by the previous results for the related compounds [84–87]. The formation of aggregates seems to be also evidenced by UV–Vis monitoring of **1–2** in phosphate buffered saline solutions (PBS) over 72 h (Fig. S9b). Over the entire spectral range, the reduction in the absorbance occurred due to formation of precipitates of **1–2**. With the reference to the previous studies, however, hydration process in PBS cannot been excluded [88,89]. On the contrary, no spectral changes were observed for 72 h in the diluted dimethyl sulfoxide (DMSO) solution of **1–2** (10–50 μM), confirming their stability in these conditions (Fig. S9b).

In analogy to the parent [PtCl(terpy)](SO$_3$CF$_3$) [53,84,85] and other related [PtCl(4′-R-terpy)]X [90], the complexes **1–2** were found to be non-emissive in diluted (12.5 μM) DMSO solution at ambient conditions, most probably due to the thermally activated population of ^{3}MC excited state. Emission maxima of the free ligands 4′-R^1-terpy and 4′-R^2-terpy in DMSO occur at 356 and 353 nm, respectively. Additional data concerning emissive properties of **1–2** in solid state and low temperature (77 K) are available in ESI (see Figs. S10–11 and Table S8).

2.2. DNA binding

The complexes **1** and **2** bear aromatic coplanar terpy-based ligand and labile chloride ion, so they are able to bind to DNA both covalently and non-covalently by intercalation [27,87,91–96]. The intercalative interaction of **1–2** with calf thymus DNA (ct-DNA) was investigated by UV–Vis absorption titration and ethidium displacement assay, while a high resolution mass study of their reactions with the model nucleobase 9-ethylguanine (9-EtG) was performed to check if Pt(II) complexes are able to bind covalently with DNA.

2.2.1. UV–vis absorption titration

Upon addition of calf thymus DNA (ct-DNA) to the solution of **1** and **2**, a slight redshift and decrease in intensity of the absorption bands corresponding to metal perturbed intra-ligand π → π* transitions was observed (Fig. S12). These spectral changes, hypochromism and bathochromic shift, are indicative for intercalative binding mode between DNA base pairs and complexes **1–2** bearing aromatic coplanar terpy-based ligand. However, in analogy to the related Pt(II) systems showing deviations from Beer's law due to formation of aggregates [97,98], the spectroscopic titration data of **1–2** cannot be fitted to a suitable binding model using the Scatchard method for the determination of K_{assoc} values (Fig. S13).

2.2.2. Ethidium bromide displacement assay

Ethidium bromide (EB) is a planar cationic dye with phenanthridine ring, which shows the enhanced fluorescence in the presence of DNA due to strong interactions between adjacent DNA base pairs *via* intercalative binding [99]. Compounds being stronger intercalators are able to displace ethidium bromide leading to decrease or quenching of the fluorescence emission.

Ethidium bromide displacement assay was carried out in PBS buffer

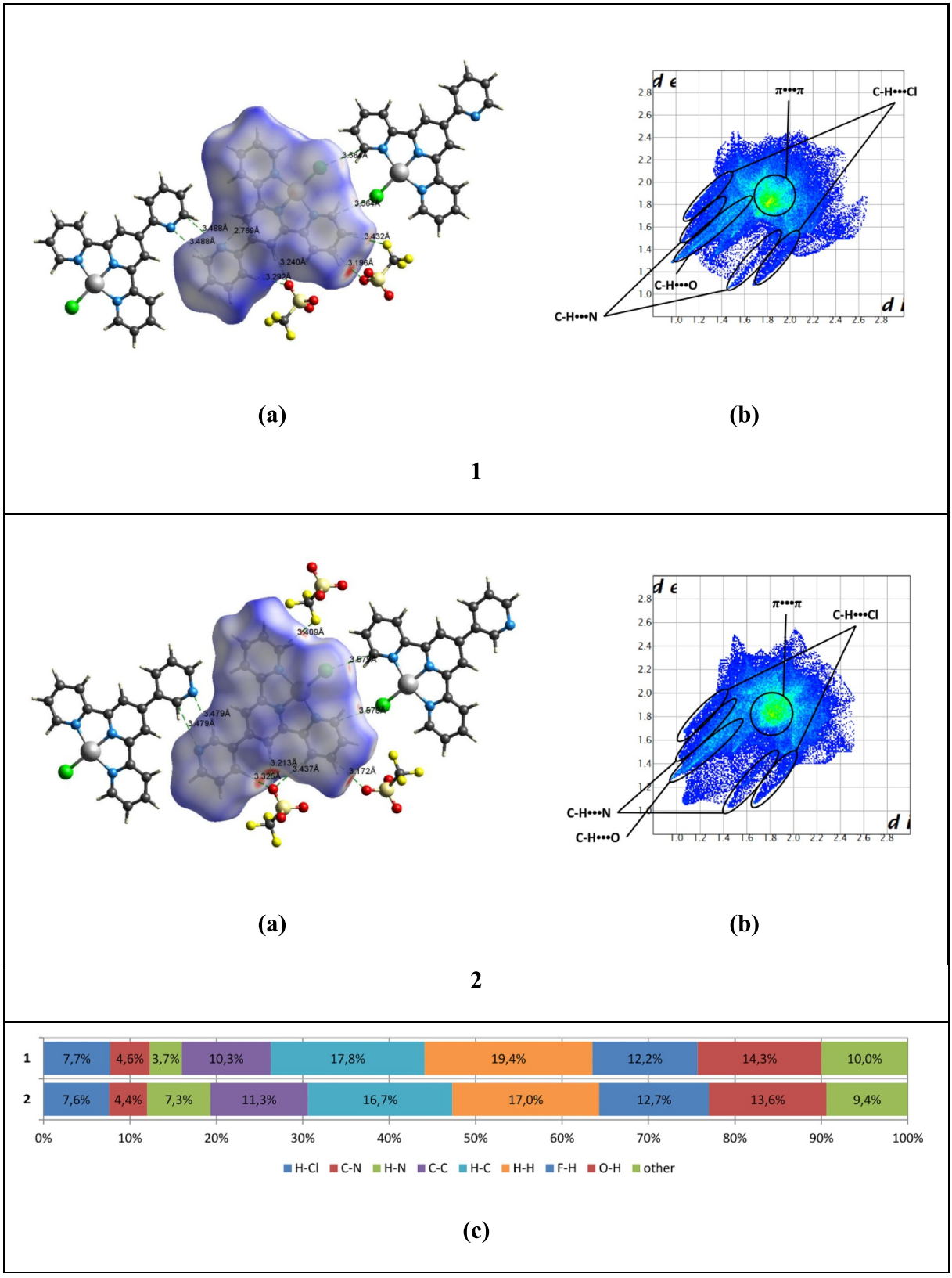

Fig. 3. Hirshfeld surface mapped with d_{norm} along with hydrogen bonds (a), and 2D fingerprint plots (b) for **1** and **2**, together with the relative contributions of various intermolecular interactions to the Hirshfeld surfaces (c).

by keeping [DNA]/[EB] = 1 ([DNA] = [EB] = 50 μM) and varying the concentrations of the Pt complexes (from 0 to 10 μM). As shown in Fig. 4, the fluorescence intensity of the EB bound to ct-DNA decreased with the increase of the compound concentration, in agreement with intercalative interactions of **1**–**2** with DNA.

The complexes showed 18% (for **1**) and 12% (for **2**) inhibition of the

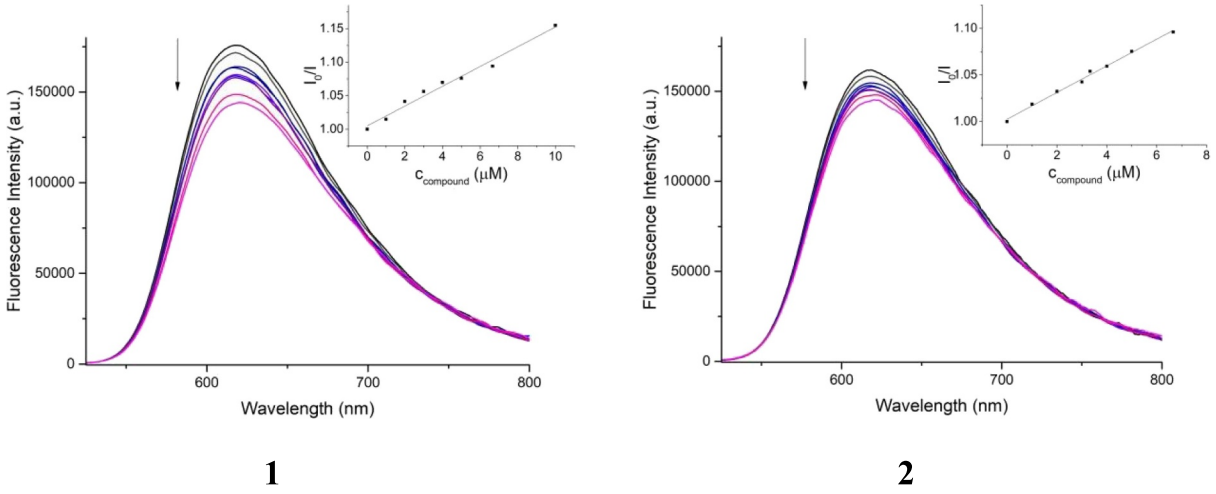

Fig. 4. Emission spectra (λ_{ex} = 510 nm) of EB–DNA in PBS buffer in the absence and presence of **1** and **2** (0–10 μM). The inset shows the Stern-Volmer plots for corresponding complexes.

EB–DNA fluorescence. The quenching constants of the Pt(II) complexes were calculated using Stern-Volmer equation [100–102]: $I_0/I = 1 + K_{SV}[Q]$, where I_0 and I are the intensities of fluorescence in the absence and presence of the complex, and [Q] is the concentration of the complex. The linear Stern-Volmer quenching constant K_{SV} is given by the ratio of the slope to the intercept in the I_0/I *versus* [Q] plot. The apparent binding constants K_{app} were calculated using equation: $K_{app}[Q_{1/2}] = K_{EB}[EB]$ [103], where $[Q_{1/2}]$ is the concentration of the quencher causing 50% reduction in the fluorescence intensity of the EB–DNA system, $K_{EB} = 1 \times 10^7\ M^{-1}$ and $[EB] = 5 \times 10^{-5}$ M.

K_{app} for complex **1** is $7.42 \times 10^6\ M^{-1}$ and $7.17 \times 10^6\ M^{-1}$ for **2**. These value is only slightly changed with 0.1 M NaCl (7.51×10^6 for complex **2**) (Fig. S14), displaying low role of ionic strength on the nature of binding. This may suggest that the external electrostatic type of binding of the Pt compounds can be ruled out, but the results should be taken with caution, since the quenching of EB–DNA fluorescence by mechanism other than intercalation is still possible.

2.2.3. Reaction with 9-Ethylguanine (9-EtG)

To gain further insights into the binding mode of platinum complexes **1–2**, particularly to assess whether they are able to bind DNA covalently besides intercalation, a high resolution mass study of their reactions with the model nucleobase 9-ethylguanine (9-EtG) was performed. Since Pt(II) belongs to the group of soft metal ion, platinum(II) compounds are known to bind preferentially to the nitrogen atoms on purine nucleobases, while binding to the sugar moiety of nucleosides is unlikely to occur. In double-stranded DNA, only N3 and N7 nitrogen atoms are not involved in Watson-Crick hydrogen bonds. However, due to the fact that N3 is sterically hindered, mainly N7 is available for coordination to Pt(II) ion. Therefore, in 9-EtG, the sugar moiety at position N9 of a purine is replaced by an alkyl group, while N3 and N7 positions remains free, which makes it a good model for evaluating the binding mode of Pt(II) complexes **1–2** to DNA.

The examined complexes were incubated with 9-EtG in DMSO over a period of 4 h and afterwards they were analyzed by high resolution electrospray ionization mass spectroscopy (ESI-HRMS). The characteristic feature of isotopic peaks distribution of complex **1**, located at about 514 *m/z*, is mainly due to the presence of both platinum and chloride atoms. Mass spectra of the product, derived from incubation with 9-EtG, showed formation of the platinated complexes. In this case, the *m/z* peaks of the 9-EtG-Pt(II) adducts correspond to the loss of the triflate group and chloride atom and the gain of an additional positive charge (z = 2), which causes that the peaks are located at the values corresponding to half of the mass of the adducts. Indeed, as reported in Fig. 5, the measured *m/z* values at around 342 and isotopic peaks distribution suggest that the cluster is formed by ions $C_{27}H_{23}N_9OPt^{2+}$, corresponding to the 9-EtG bound to **1** after removal of both counterions. Similarly, in the case of the reaction of **2** with 9-EtG, in the mass spectrum shown in Fig. 5, the measured m/z values corresponding to cluster derived from $C_{27}H_{23}N_9OPt^{2+}$ ions can be observed. However, for the quantitative analysis of covalent adducts, the more detailed studies are required.

2.3. Biological studies

2.3.1. Cytotoxicity

The cytotoxicities of the Pt(II) complexes **1–2** against HCT116, HCT116p53-/- (colon), Me45 (melanoma), A549 (lung), MCF-7 (breast) and HeLa (cervical) cancer cells and three normal ones were determined using an assay based on the conversion of MTS (3-(4,5-dimethylthiazol-2-yl)-5-(3-carboxymethoxyphenyl)-2-(4-sulfophenyl)-2H-tetrazolium) into formazan by metabolically active living cells, and they were compared with the cytotoxicities of [PtCl(terpy)](SO_3CF_3) and cisplatin used as standard anticancer drug. The half maximal inhibitory concentration (IC_{50}) with SD (standard deviation) were determined from the dose-dependence of surviving cells after exposure to platinum(II) complexes for 72 h (Fig. S15) using GraphPad Prism 6.05 software (Table 1). In general, for the compound **2**, the IC_{50} values towards all the cancer cell lines are in the low micromolar range. Compound **1** shows $IC_{50} > 10$ μM and is equally cytotoxic in non-malignant cells. For all the cancer cell lines except HeLa, the compounds **1** and **2** are more active than [PtCl(terpy)](SO_3CF_3) and cisplatin, and **2** is much more cytotoxic compared to **1** demonstrating crucial role of the position of the nitrogen atom in the pendant substituent. Against A549 cells, **2** is over 4 times more effective than **1** and cisplatin. At the same time, the selectivity index of **2** is ~60–80 times higher than that for **1** and cisplatin.

For HeLa cells, cisplatin was found to be more active than **1** and [PtCl(terpy)](SO_3CF_3), while the cytotoxicity of **2** was comparable to cisplatin. The striking difference between **2** and cisplatin against HeLa cells concerns the selectivity index, which is ~15 times higher in the case of **2**. To get a deeper insight into the mechanisms underlying the loss of viability under treatment of **2**, a more detailed investigation was performed for this compound.

2.3.2. Impact on actin cytoskeleton and cell morphology

It is known that actin cytoskeleton plays a crucial role in maintaining cell shape, as well as it affects the cell adhesion and motility

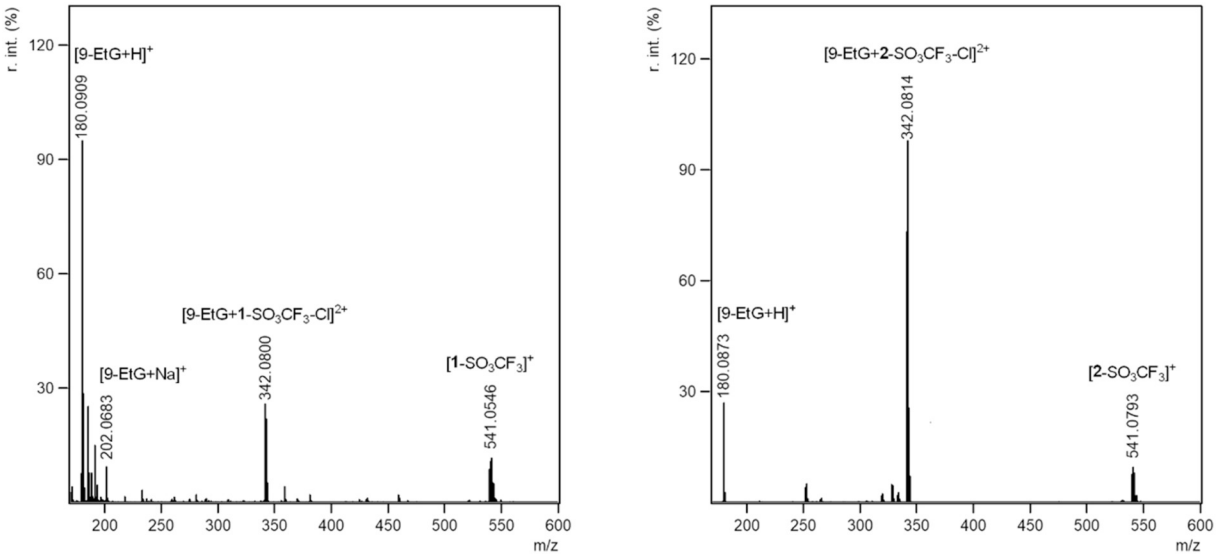

Fig. 5. Mass spectra of the 9-EtG incubated with platinum complexes **1** and **2**. Final concentration in DMSO before injection were 0.2 mM for **1**–**2** and 0.8 mM for 9-EtG.

[104,105]. To assess the influence of **2** on the actin cytoskeleton integrity and cell morphology, F-actin staining was used. The control cells exhibited the shape typical for A549 line, and actin cytoskeleton with well-developed stress fibers and multiple focal adhesions was clearly visible (Fig. 6c, g, j, n, p). In the population of the cells treated with **2** for 3 h, the elongated cells (Fig. 6a) and contracted cells with condensed cytoplasm, indicative for some features of apoptosis (Fig. 6b), appeared among the cells with normal morphology. Similar alterations were visible in the case of 6-h treatment, but cells of elongated shapes (Fig. 6d) or showing shrinkage (Fig. 6e) seemed to be much more frequent. The elongated cells, despite the altered morphology, preserved roughly normal actin cytoskeleton with distinct bundles of microfilaments (Fig. 6a, d, h, i, k), whereas the shape of the contracted cells with condensed cytoplasm was more rounded and microfilaments were poorly visible (Fig. 6b) or almost completely depolymerized (Fig. 6e). For longer 24-h and 48-h treatment, only elongated cells, sometimes with long cytoplasmic tails (Fig. 6h, k, arrows), were present in the cell population. On the other hand, the vast majority of the cells exhibited normal morphology and correct actin cytoskeleton organization in the case of 72-h treatment (Fig. 6n, o).

To sum up, the tested compound **2** has shown to have the biggest impact on cell morphology in the case of 6-h treatment, leading to the changes in cell morphology, but without triggering direct depolimerization of actin microfilaments.

2.3.3. Cell cycle

The cytometric cell cycle analysis was performed on a A549 cells treated with the compound **2** at IC_{50} dose for a maximum of 96 h, and the cells were harvested at appropriate times (1, 3, 6, 12, 24, 48, 72 and 96 h). In parallel, the analysis was carried out against a non-synchronized control A549 cells. It resulted in standard histograms with three cellular fractions: G0/G1 for diploid cells (2n); S for DNA replication and G2/M for mitotic cells (4n). In comparison to the control A549 cells, the treated cells kept their cycle unchanged during the first 3 h, and from that point they responded with G0/G1 inhibition. A strong cycle block in the G0/G1 phase lasts up to the end of the observations. For better visualization of the cell cycle arrest and showing G0/G1 fraction domination, the G1/G2 ratio was calculated across the time-points 1–96 h (Fig. 7).

Statins-like drugs (cyto-statins) effectively influence cell cycle, both

Table 1
Cytotoxicity of the studied compounds towards cancer cell lines and normal cells determined by the MTS assay and presented as the IC_{50} value with SD (the incubation period of 72 h). The selectivity index (SI) was calculated as sum of IC_{50} mean values for NHDF, BEAS-2B and GM07492 cells/mean IC_{50} value for a particular cancer cell line and marked with *. #Data from ref. [42].

		Compound			
		1	**2**	[PtCl(terpy)](SO_3CF_3)	Cisplatin
Cancer cells	HCT116 [μM]	30.92 ± 10.40	4.49 ± 0.34	45.74 ± 2.52	20.30 ± 2.80#
		*0.69	*67.14	*1.27	*0.88
	HCT116p53$^{-/-}$ [μM]	20.39 ± 2.08	4.21 ± 0.28	62.19 ± 2.73	31.99 ± 5.82#
		*1.04	*71.65	*0.93	*0.56
	Me45 [μM]	29.48 ± 4.72	9.02 ± 1.05	120.30 ± 6.82	11.50 ± 0.84
		*0.72	*33.43	*0.48	*1.55
	A549 [μM]	11.33 ± 2.78	2.64 ± 0.73	> 50.00	12.82 ± 0.99#
		*1.87	*114.33	*1.16	*1.39
	MCF-7 [μM]	8.34 ± 2.58	4.60 ± 1.24	49.42 ± 5 0.90	14.99 ± 2.09#
		*2.54	*65.54	*1.18	*1.19
	HeLa [μM]	77.69 ± 16.37	20.56 ± 2.58	83.17 ± 4.28	19.02 ± 2.00
		*0.27	*14.66	*0.70	*0.94
Normal cells	NHDF [μM]	28.86 ± 2.90	126.80 ± 48.24	43.71 ± 5.90	12.31 ± 1.51#
	BEAS-2B [μM]	7.44 ± 1.34	4.32 ± 0.98	80.91 ± 8.74	12.46 ± 1.15#
	GM07492 [μM]	27.35 ± 6.78	773.00 ± 353.60	> 50.00	28.75 ± 3.68

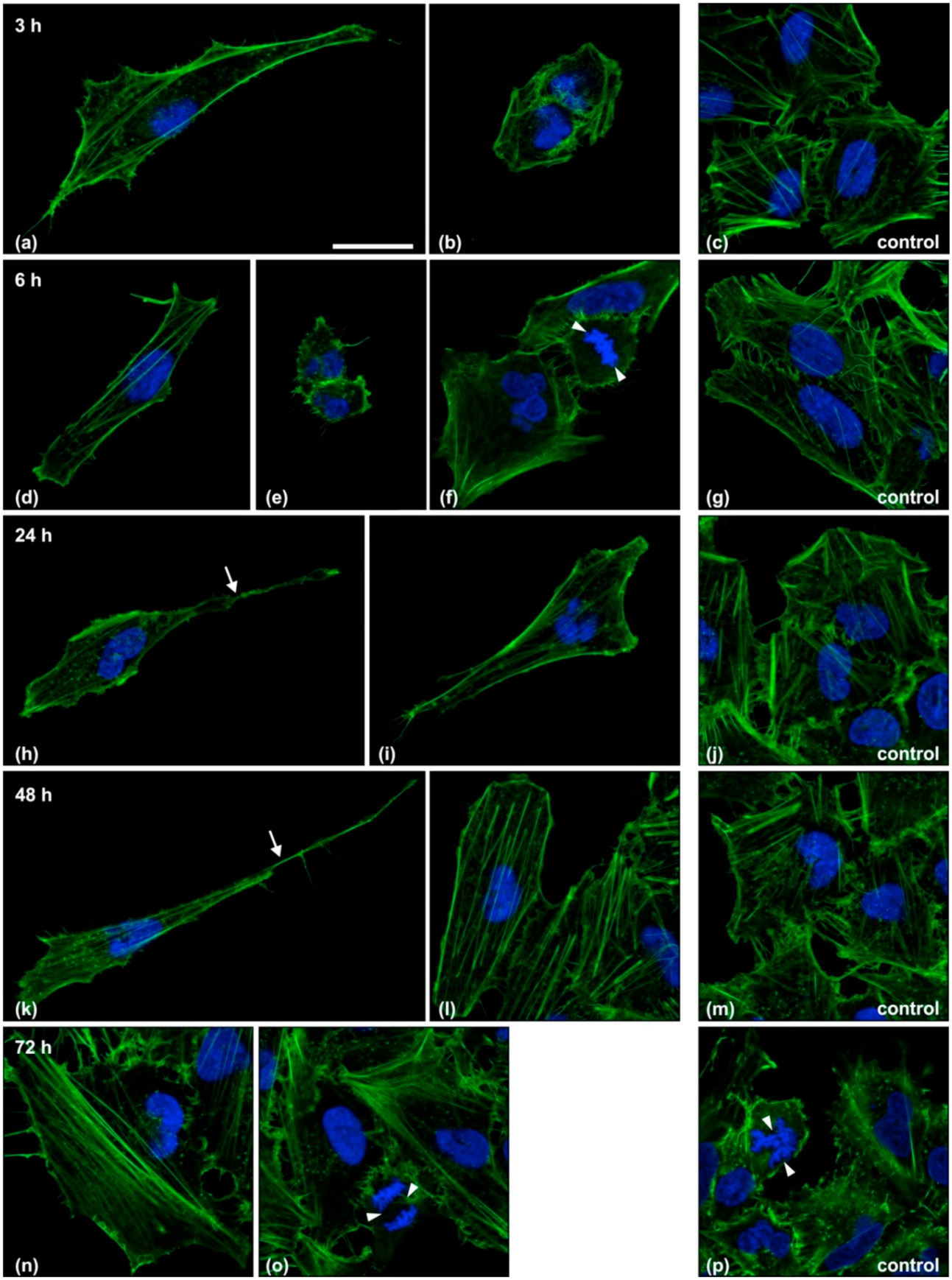

Fig. 6. Actin cytoskeleton organization and cell morphology in the populations of cells treated with **2**. F-actin shown in green and DNA – in blue; long cytoplasmic tails sometimes visible in cells treated with **2** are marked by white arrows; cells during division are marked by white arrowheads; scale = 25 μm. (For interpretation of the references to colour in this figure legend, the reader is referred to the web version of this article.)

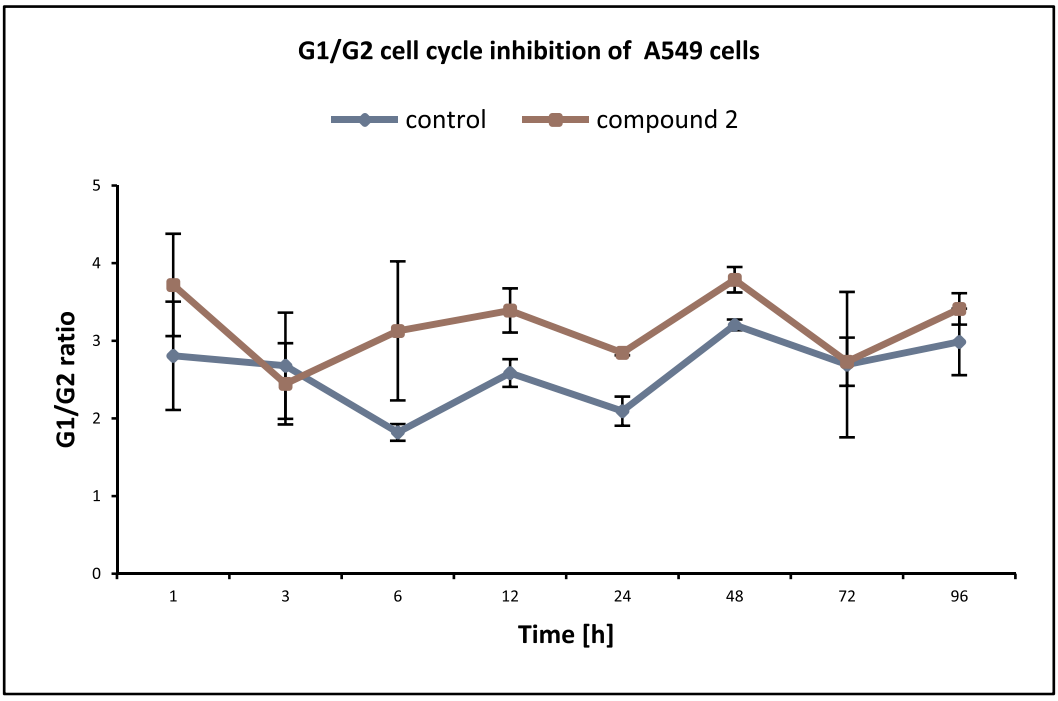

Fig. 7. Cell cycle inhibition after compound **2** at IC_{50} dose treatment. Ratio of G1/G2 express a blockade in cell cycle at G0/G1 phase, cells are mainly presented as mononuclear (diploid cells = 2n) and didn't proceed cell cycle to S or G2/M phase, respectively.

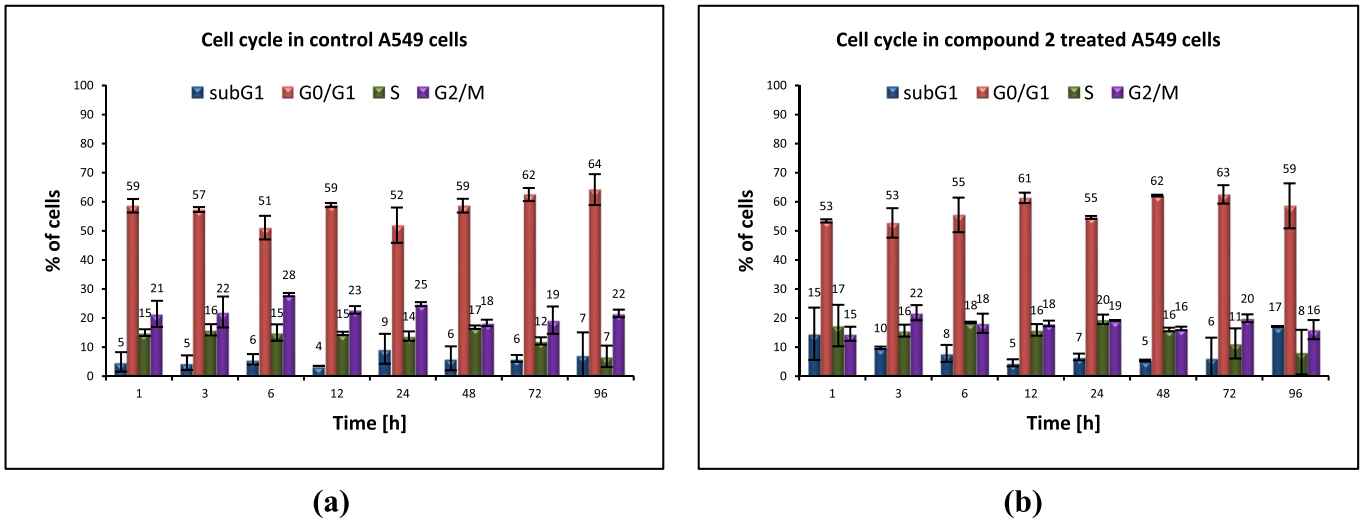

(a) (b)

Fig. 8. Cell cycle after compound **2** at IC_{50} dose treatment. Flow cytometry measurements from each time-points collected A549 cells with sub-fraction distributions after DNA-content analysis in control (a) and treated cells (b).

on the interphase (mono-nucleated cells at phase G0/G1 or DNA replicated phase S) or mitosis (bi-nucleated cells at phase G2/M), what means arrest of the cell cycle progression at check-points level and blockade at the specific stage of cells division process. Some of the statins block the cell cycle at G0/G1 stage, and during cell cycle analysis mostly mono-nucleated cells are observed. After A549 cells treatment with compound **2** at IC_{50} dose, the phase of G0/G1 was not dominated during the observation. Compared to the untreated controls (Fig. 8), however, the S and G2/M phases decreased, indicating arrest of the cell cycle. Ratio of G1/G2 phases at each time-point relative to the controls confirms the inhibitory effects of **2** on A549 cell cycle (Figs. 7 and 8). As a consequence, an S-phase un-propagation and G2/M phase decrease are observed. The DNA replication (S-phase) could not be propagated without earlier and effective DNA repair.

2.3.4. *Apoptosis analysis*

Additional apoptosis analysis, followed by fluorescein isothiocyanate (FITC) -conjugated Annexin V antibody and propidium iodide (PI) staining, allowed us for cytometric cells observations and simultaneous discrimination of normal (Annexin V negative and PI negative), early-stage of apoptotic (Annexin V positive and PI negative), late apoptotic (Annexin V positive and PI positive), and necrotic (Annexin V negative and PI positive) cells. Addition of **2** in an IC_{50} dose to A549 cells did not result in changing the dead cell population relative to its proportion in the untreated cells, determined by Annexin V apoptosis assay (Fig. 9a and b). Neither pro-apoptotic nor pro-necrotic effects were observed in A549 cells treated with **2**, which was also evidenced by cytometric measurements for mass and mitochondrial potential. Canonical apoptosis pathway was not induced, so the

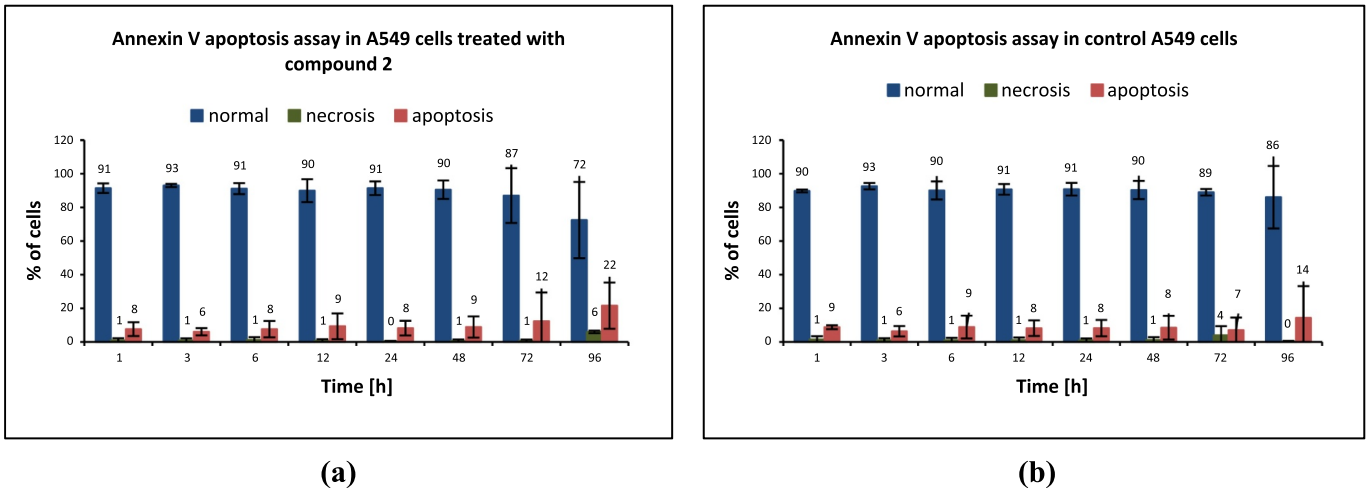

(a) (b)

Fig. 9. Cellular death after treatment by **2** at IC_{50} dose, during long term observations by Annexin V apoptosis and PI necrosis assay of control (a) and A549 treated cells (b).

compound **2** seems to be ideal cytostatic agents, with pro-oxidative (Fig. 9) and anti-proliferative activity (Figs. 7 and 8).

2.3.5. Impact on mitotic index and presence of micronuclei

In order to check if the mitotic blockage takes place in A549 cells treated with the **2** mitotic index was quantified. The analysis showed that the percent of the dividing cells is generally lower in the case of the treated cells (Fig. 10). The difference in mitotic index between the treated and control cells was especially pronounced in the case of treatments lasting 6 h and 48 h, with the statistical significance $p < 0.005$ and $p < 0.05$ respectively. As shown by the phase indices (Table 2), in the case of 6-h treatment, significantly less cells in metaphase and anaphase/telophase was scored, whereas for 48-h treatment, statistically significant differences were obtained for prophase/prometaphase. These results confirmed that the compound **2** does not block cells during cell division, but rather inhibits the cell cycle before mitosis.

The morphological cell analysis revealed the presence of small chromosome fragments in the dividing cells treated with **2** (Fig. 6f, arrowheads). In the next stage, such microstructures can form micronuclei, which are commonly known as indicators of genotoxic agents [106,107]. To assess the potential genotoxicity of **2**, a more systematic analysis of the micronuclei was performed. It showed that the number of cells with micronuclei was generally higher for the treated cells than the control ones (Fig. 11). The difference was especially prominent for 6-h treatment, for which the cells with one or two micronuclei were much more frequent compared to the control population. It is also worth mentioning that the cells with three or more micronuclei were never observed in the control population, whereas they occurred among treated cells after 6-h and 48-h treatment (Fig. 11). Therefore, it can be supposed that the compound **2** affects the genetic materials of the cells.

2.3.6. Analysis of the level of reactive oxygen species

The intracellular ROS level was determined using 2′,7′-dichlorodihydrofluorescin diacetate (DCFH-DA) for the control A549 cells and those treated with **2** at an IC_{50} concentration. DCFH-DA becomes a

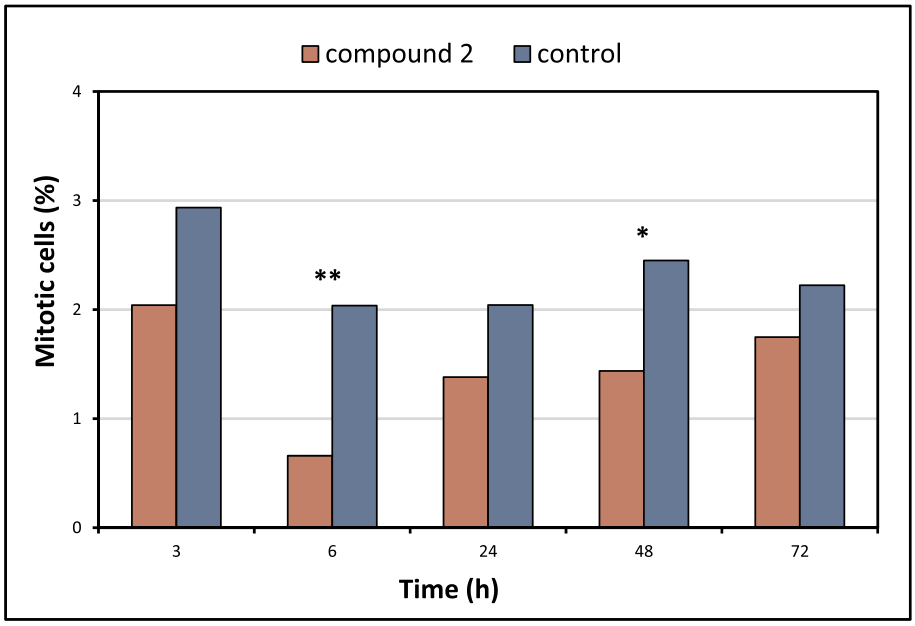

Fig. 10. Mitotic index in the populations of cells treated with **2**. Statistically significant differences are marked by asterisks (* - $p < 0.05$; ** - $p < 0.005$; chi-square test).

Table 2
Phase indices in the populations of cells treated with **2**. Asterisks mark the values which were significantly lower in the treated cells in comparison to control cells (* - $p < 0.05$; ** - $p < 0.005$; chi-square test).

Time (h)	Phase index (%)					
	Prophase/prometaphase		Metaphase		Anaphase/telophase	
	Treated	Control	Treated	Control	Treated	Control
3	0.17*	0.85	0.94	1.33	0.94	0.76
6	0.38	0.55	0.19*	0.78	0.09*	0.71
24	0.28	0.44	0.46	0.95	0.64	0.66
48	0.17**	0.88	0.83	0.99	0.44	0.58
72	0.63	0.81	0.70	0.94	0.42	0.47

highly fluorescent probe upon deacetylation by intracellular esterases and oxidation by ROS. It can be detected by fluorescence spectroscopy with excitation/emission at 495 nm/529 nm, and it is a quantitative method for oxidative stress assessment, mainly hydroxyl, peroxyl and other ROS activity within the cell.

Addition of compound **2** at IC_{50} dose influenced a ROS production in A549 cells during long-term observations (1–96 h). Physiological level of ROS in the control cells comes mostly from oxidative phosphorylation in mitochondria, β-oxidation of lipids, proteins peroxidation in proteasomes and other endogenous cellular processes. Addition of any external stimulators, such as pro-oxidative drugs, impacts the sensitive oxidative homeostasis in the cells. A slight increase (116%) in the production of free radicals in the cells treated with **2** begins in the third hour of incubation and reaches a maximum value after 6 h (296%). This ROS overproduction and oxidative stress lasted up to 12 h (138%). All that ROS accumulations may result from oxidative and toxic effects of the tested compound, which displayed a direct and pro-oxidative activity at IC_{50} dose (Fig. 9). Microscopic observations and cell cycle analysis for control and treated cells revealed that the compound **2** leads to chromosomes and DNA damage with micronuclei accumulation, and G1 cell cycle arrest (Figs. 7, 10, 11). After 24 h, the oxidative stress in the treated cells was silenced, and the ROS production was suppressed below the control cells (42%). Another, secondary ROS burst was recorded at the 72 h incubation. It could be an effect of cell cycle arrest, which is still observed even up to 96 h (Fig. 12).

2.3.7. *The mass of mitochondria and the mitochondrial potential $\Delta\Psi_m$*

To explain the mechanism of cell cycle arrest and ROS production under the effect of the compound **2**, and the fact that the compound did not cause death by apoptosis or necrosis pathway (lack of higher than in controls sub-G1 phase on the cell cycle analysis; Figs. 7 and 8), the analysis of changes in the mitochondrial mass and potential (Fig. 13) was performed.

The cell multiplies by subjecting to an ordered sequence of events, during which it first doubles its content and then divides into two new cells. In most cases, in each cell cycle, cells also multiply their organelles and macromolecules, using additional time for the growth and multiplication that the G1 and G2 phases provide. Otherwise, they would become smaller after each division. Thus, dividing cells must also coordinate growth with division to maintain their size as well. In the cells treated with **2**, slight oscillations were observed in the mass of mitochondria. The behavior of cells in the cell cycle and the block in the G0/G1 phase indicate that these cells partially began the duplication process of mitochondrial but through the arrest they were arrested in this phase (started from 6 h), they were not able to significantly increase the number of these organelles. In the first 6 h, the value (125%) of the mitochondrial mass of cells treated with the compound **2** was slightly above the control. In 12 to 48 h the number of mitochondria did not change with respect to control cells (87%–100%), and finally within 72–96 h, the cells increased number of mitochondria (125%–131%). However, these changes are statistically insignificant. The cell cycle check-points, and cyclines which stimulated cycline-dependent kinases (CDKs), are necessary for cell cycle propagation and phases switching. Although mitochondria are known as autonomic organelles, their proliferation is generally synchronized in time with the main cell cycle.

Despite cell cycle blockade in G0/G1 phase, mitochondria division

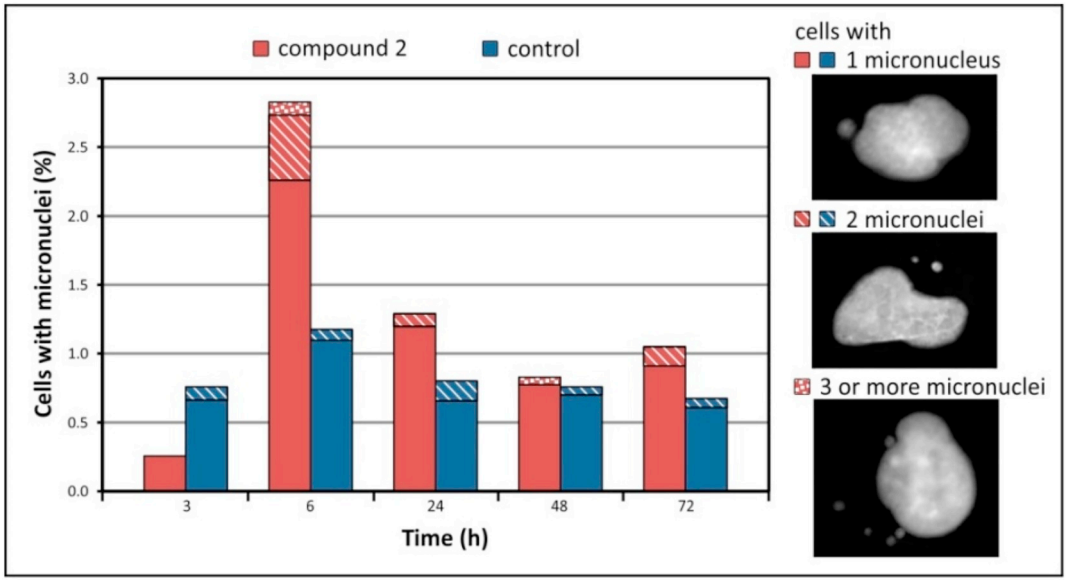

Fig. 11. The percent of cells with micronuclei in the populations of cells treated with **2** in comparison to control cells.

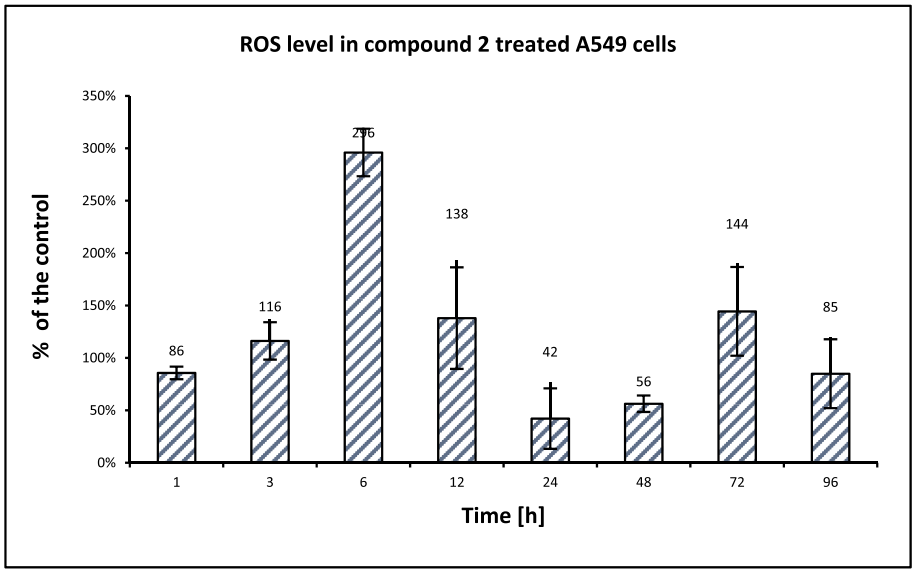

Fig. 12. Time-dependent ROS production after the treatment of A549 cells with compound **2**. Results obtained from three independent experiments in triplicate, and presented as mean ± SD.

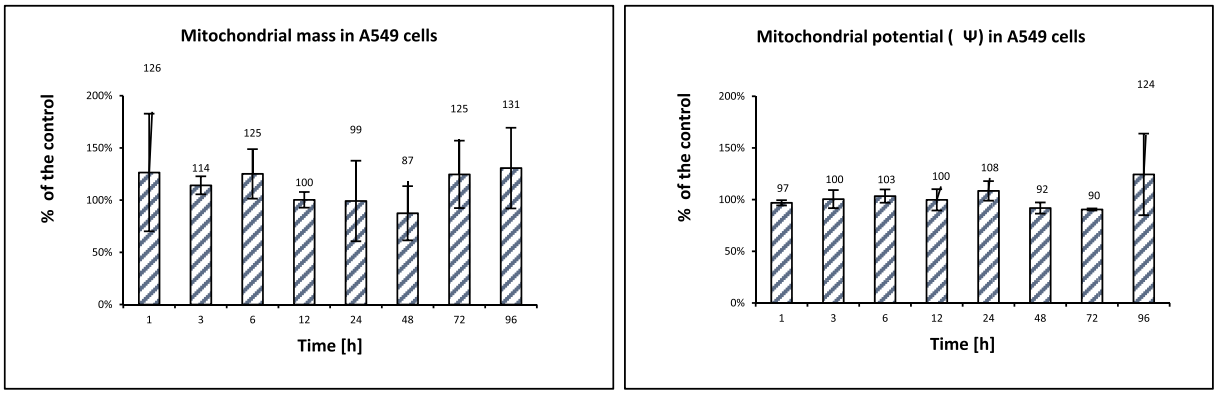

(a) **(b)**

Fig. 13. Time-dependent changes in mitochondrial mass (a) and potential (b) in A549 cells after the treatment of **2**. Results obtained from two independent experiments in triplicate, and presented as mean ± SD.

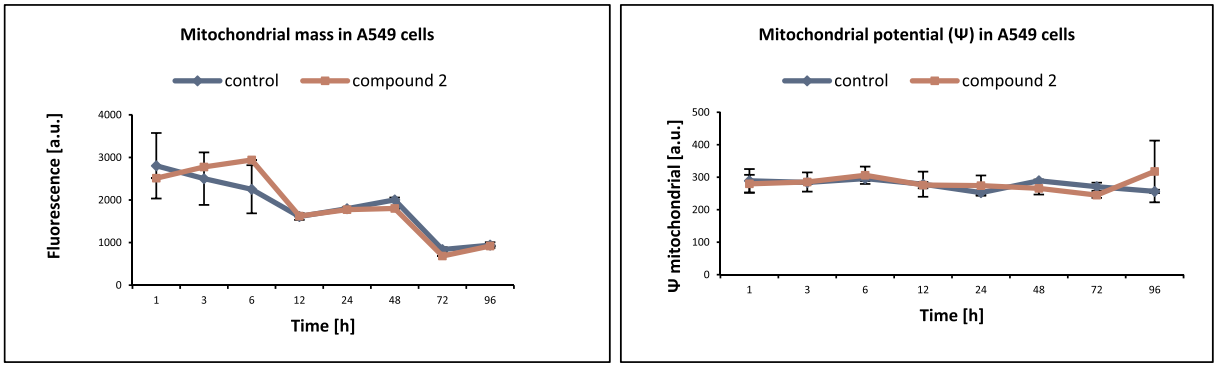

(a) **(b)**

Fig. 14. Time-depended changing in mitochondrial mass (a) and potential (b) of control A549 and treated cells with **2** at IC_{50} dose.

is still occurred in A549 cells after addition of **2** (Fig. 13a). Strong cell cycle arrest (Fig. 9) and ROS accumulation (Fig. 12) confirm the hypothesis that compound **2** is a pro-oxidative with direct (first significant effects at 6 h) and anti-proliferative (cytostatic) activity drug. For better visualization of subtle changes in mass and mitochondrial potential in the treated A549 cells in comparison to the control ones, the raw data of fluorescence [a.u] from flow cytometry analyses were presented (Fig. 14). Changes between both cells sub-population during long-term

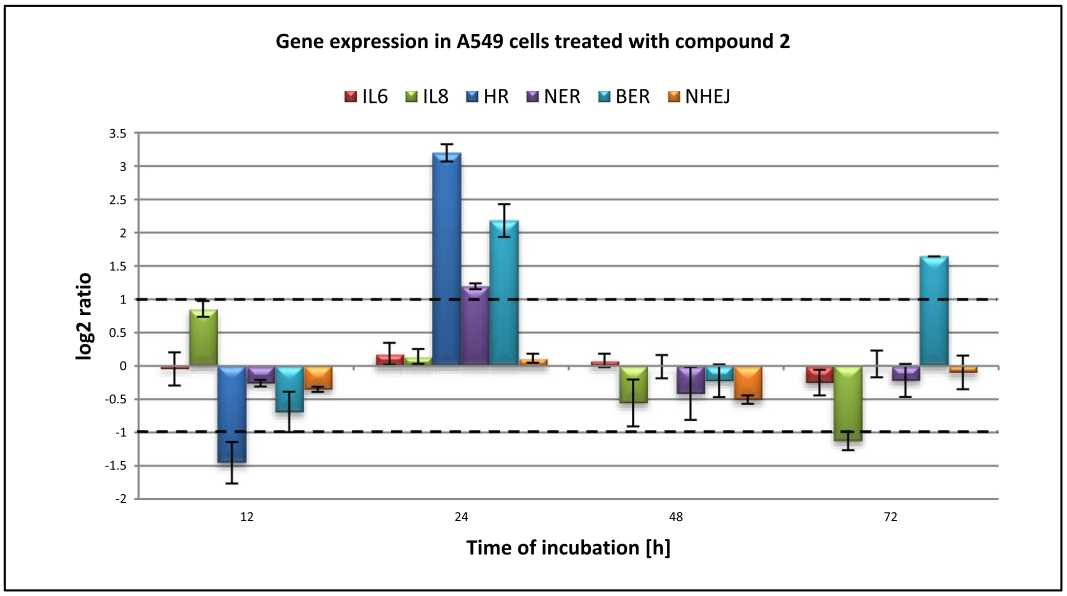

Fig. 15. qRT-PCR array analysis and validation of results. Gene expression analysis in A549 cell line treated with **2** at a IC_{50} concentration for 12, 24, 48 and 72 h. The diagram shows log2 ratio for all 6 tested genes (IL-6, IL-8, HR, NER, BER, NHEJ). Results obtained from three independent experiments in triplicate, and presented as mean ± SD.

observations (1–96 h) were rather insignificant and the profiles of mass and mitochondrial potential were similar after treatment of the compound **2** at IC_{50} dose.

2.3.8. Molecular mechanism of A549 cells response to treatment

We analyzed expression of six different genes using quantitative real time polymerase chain reaction (qRT-PCR) analysis. A549 cells were treated with **2** at a concentration equal to the IC_{50}, and time of incubation was: 12, 24, 48 and 72 h (Fig. 15). There is a good agreement between the cell cycle and qRT-PCR results. Interleukin 8 (IL8), whose expression in tumor cells is large, decreases after 24 h, which causes the decline of the proliferation ability. We did not observe necrotic effects, therefore, up or down regulation of interleukin 6 (IL-6) expressions almost does not exist. We also analyzed genes expression from specific DNA damage and repair pathways: gene ERCC3 from NER (Nucleotide Excision Repair); OGG1 from BER (Base Excision Repair); XRCC4 from NHEJ (Non-Homologous End Joining) and RAD51 from HR (Homologous Recombination). After 24 h, HR, NER and BER were activated; expression of marker genes increased, which means that repair pathways related to damaged nitrogenous bases (oxidation) and whole nucleotides (AP-sites) were turned on. There was no activation for the repair of broken DNA strands (DNA single- or double stranded breaks), signaling that the expression of genes responsible for repair enzymes from the NHEJ pathway were not activated. The action of the compound **2** as cytostatic agent, without apoptosis/necrosis activation, differs from well-known cisplatin, which acts mainly on the S-phase of cancer cells and inhibits the DNA replication, leading to stop cell proliferation. The compound **2** acted on A549 cells on G1 phase and did not propagate the cell cycle to next S-phase, that there was no DNA replication after treatment with **2** at IC_{50} dose. After 72 h, BER was upregulated which is correlated with secondary explosion of ROS – most likely due to oxidative damage of nitrogen bases were still present in nucleotides. The compound **2** acts as anti-proliferative agent and effectively blocks the cell cycle, in agreement with measurements of cells viability by MTS assay, leading to decrease in mitochondrial activity. The lower viability of cells treated with compound **2** than control cells resulted from cell cycle arrest, not only from cells death.

3. Conclusions

The structural, photophysical and biological properties of two Pt(II) complexes bearing 4′-(2-pyridyl)-2,2′:6′,2″-terpyridine (4′-R^1-terpy) and 4′-(3-pyridyl)-2,2′:6′,2″-terpyridine (4′-R^2-terpy) were discussed depending on the pendant substituent and compared with those reported for related [Pt(terpy)Cl]X and cisplatin. The striking difference between **1** (with 4′-R^1-terpy) and **2** (4′-R^2-terpy) concerns their cytotoxicity. Against A549 cells, **2** is almost 4 times more effective than **1** and cisplatin, while the selectivity index of **2** is ~60–80 times higher than that for **1** and cisplatin.

The compound **2** was found to have the biggest impact on A549 cells morphology in the case of 6-h treatment, leading to the changes in cells morphology, but without triggering direct depolimerization of actin microfilaments. The mitotic index indicates that **2** does not block cells during cell division, but rather inhibits the cell cycle before mitosis. A strong cycle block in the G0/G1 phase starting at 3 h on A549 cells treated with **2** was confirmed by the cytometric cell cycle analysis. Compound **2** has a pro-oxidative effect by strong stimulation of cells for the production of reactive oxygen species and cytostatic effect, through cell cycle arrest, but not pro-apoptotic one, as demonstrated by the cytometric analysis and evaluation of the mitochondrial status. Also, a decrease of the level of IL8 after 24 h confirms a decrease in the ability of the cells treated with **2** to proliferate. On the basis of qRT-PCR results, necrotic effects can be excluded as up-regulation or down-regulation of IL-6 expression is almost non-existent. The activation of HR, NER and BER after 24 h indicates that repair pathways associated with damaged nitrogenous bases (oxidation) and entire nucleotides (AP sites) are induced.

The mixed nature of the interactions of the test compound with DNA, through covalent linking and direct intercalation, was also demonstrated. This mechanism, as well as the biological effects caused by **2**, such as high cytostatic activity and selectivity of action, cause that it may become an alternative to the classical cisplatin in the future.

4. Experimental

4.1. Materials and methods

All reagents used for the syntheses of the coordination compound

are commercially available and have been used without further purification. The $[Pt(PhCN)_2Cl_2]$ starting compound was obtained from Strem Chemicals Inc. The terpyridine ligands: 4′-(2-pyridyl)-2,2′:6′,2″-terpyridine (4′-R^1-terpy) and 4′-(3-pyridyl)-2,2′:6′,2″-terpyridine (4′-R^2-terpy) were synthesized according to procedures described previously in the literatures [80,90,108–110].

Infrared spectra were recorded on a Nicolet iS5 FT-IR spectrophotometer in the range 4000–400 cm^{-1} using KBr pellets. Electronic absorption spectra were measured on a Nicolet iS50 UV-VIS-NIR spectrophotometer in the range of 600–180 nm in acetonitrile solutions. The solid state spectra were made for powder samples with use of the 60 mm Spectralon® integrating sphere and the measured reflectance was set to absorbance. High resolution mass spectrometry (HRMS) analyses were performed on a Maxis Impact Bruker mass spectrometer equipped with an electrospray (ESI) ion source and a quadrupole time-of-flight (Q-TOF) mass analyzer. Analyzed samples were dissolved in CH_3CN. Full-scan MS data were collected from 50 to 1300 *m/z* in positive ion mode and the data was calibrated using sodium formate (Sigma Aldrich). The recorded data were processed using Data Analysis 4.1 software. The ^1H and ^{13}C NMR spectra were obtained at room temperature in $CDCl_3$ using a Bruker 500 MHz spectrometer. Elemental analyses (C, H, N) were performed on a Perkin–Elemer CHN–2400 analyzer.

The photoluminescence spectra were undertaken on the FLS − 980 spectrophotometer. The room-temperature spectra were prepared in diluted solutions and solid state (powder). The low-temperature emission spectra were measured in ethanol:methanol mixture (4:1) frozen-glass matrix at temperature of liquid nitrogen with Dewar assemble.

The time-resolved measurement was carried out at optically diluted ($0.05 < O.D < 0.1$) solutions at room and low temperature using the time correlated single photon counting methods (TCSPC) on the FLS-980 spectrophotometer. Excitation wavelengths were obtained using the set of picosecond pulsed diodes (EPL-405 nm) or microsecond lamp as light sources and PMT + 500 nm (Hamamatsu, R928P) in cooled housing was used as a detector. The system was aligned at the emission wavelengths. Additionally, for the analysis of a fluorescence decay, an instrument response function (IRF) was obtained. The IRF contains the information about the time response of the overall optical and electronic system. The IRF was designated using Ludox® solution as a standard at excitation wavelengths.

The quantum yields were examined in solution and solid phase using integrating sphere direct method. The solvent and Spectralon® reference standard were used as blanks, respectively in the case of diluted solutions and powder samples. The compounds were excited with wavelength in each case corresponding to the obtained excitation bands. The FLS-980 software was used to designate the quantum yield values.

Cyclic voltammetry (CV), differential pulse voltammetry (DPV) measurements were carried out on the Autolab potentiostat (Eco Chemie). A three-electrode one-compartment cell was used to contain the solution of complexes and supporting electrolyte in CH_3CN. Deaeration of the solution was achieved by argon bubbling through the solution for about 10 min before measurement. The complexes and supporting electrolyte ($n\text{-}Bu_4NPF_6$) concentrations were equal to 0.00005 and 0.01 M, respectively. The scan rate was equal to 0.1 V/s. A glassy carbon disk working electrode (3 mm diam.), and an Ag/Ag^+ reference electrode were used. All electrochemical experiments were carried out under ambient conditions.

The experiments involving DNA binding were carried out in Dulbecco's Modified Phosphate Buffered Saline (PBS, pH 7.4, Sigma-Aldrich) at 20 °C. Calf thymus DNA (ct-DNA) was obtained from Sigma-Aldrich. The concentration of ct-DNA was determined by UV absorbance at 260 nm, with the molar absorption coefficient $\varepsilon_{260} = 6600\ M^{-1}\ cm^{-1}$ [111]. Solution of ct-DNA in PBS gave a ratio of UV absorbance A_{260}/A_{280} of approximately 1.85, indicating that the DNA was sufficiently free of protein [112]. The DNA concentration was measured by using NanoDrop™ 2000/2000c Spectrophotometer (Thermo Fisher Scientific™). Stock solution of DNA was stored at 4 °C for no longer than 4 days before use. Concentrated stock solutions of metal complexes were prepared by dissolving the complex in 0.1 ml of DMSO and diluted suitably with PBS buffer to required concentrations for all the experiments.

The absorption spectra were recorded on a HITACHI U-2900 UV–Vis spectrophotometer. Absorption titration experiments were performed by addition of increasing amounts of the ct-DNA solution while keeping a constant concentration of the compound (25 μM). The mixtures of compound/ct-DNA were well mixed and immediately measured. The concentration of the ct-DNA varied from 0 to 3.00 mM. Absorption spectra were obtained in range 220–500 nm. ESI-HRMS spectra were recorded on a Mass Spectrometer AB Sciex 4000 QTRAP operated in positive-ion mode. Fluorescence quenching experiments were carried out using ethidium bromide (EB) fluorescence displacement assay with spectra recorded using FLS-980 spectrophotometer. Equimolar amount (50 μM) of EB solution was added to ct-DNA solution at room temperature, followed by 2 h incubation in the dark. The compound was then titrated into the EB–ct-DNA mixture, well mixed and allowed to stand for 30 min. The concentration of the complexes varied from 0 to 10 μM. Fluorescence spectra of EB bound to DNA were obtained at excitation wavelength of 510 nm and emission wavelength of 618 nm.

4.2. Synthesis

A suspension of $[Pt(PhCN)_2Cl_2]$ (0.10 g, 0.21 mmol) in acetonitrile (10 ml) was treated with an equimolar amount of $Ag(CF_3O_3S)$ (0.054 g, 0.21 mmol) dissolved in acetonitrile (5 ml). The reaction mixture was heated under reflux for 16 h in the dark, the AgCl precipitate was removed by filtration and one equivalent of ligands was added to the filtrate. The reaction mixture was heated into solvatothermal reactor under atmospheric pressure for an additional 24 h and then gradually cooled by another 24 h. The crystals suitable for X-ray analysis were obtained directly from reaction mixtures.

***1*: Yield 67%**. $C_{20}H_{14}ClN_4Pt$, CF_3O_3S. **Anal**. calcd: C 36.56% H 2.05% N 8.12% found: C 36.60%, H 2.15%, N 7.99%. **HRMS (ESI)**: calcd for $C_{20}H_{14}ClN_4Pt$ 540.0551 found 540.0559. **IR (KBr; cm^{-1})**: 3441 $\nu_{(OH)}$; 3077 $\nu_{(ArH)}$; 1607 $\nu_{(C=N,\ C=C)}$; 1477, 1408 $d_{(C–CH\ out\ of\ the\ plane)}$; 1262 $\nu_{as(SO3)}$; 1150 $\nu_{(C–N)}$; 1095 $\delta_{(C–CH\ in\ the\ plane)}$; 1030 $\nu_{s(SO3)}$; 782 $\delta_{(C–C\ out\ of\ the\ plane)}$; 661 $\delta_{(C–C\ in\ the\ plane)}$; 638 $\delta_{(SO3)}$. **^1H NMR (400 MHz, DMSO)** δ 9.19 (s, 2H, H^{B2}), 8.92–8.89 (m, 3H, H^{A1} **and** H^{C5}), 8.84 (d, J = 7.9 Hz, 2H, H^{A4}), 8.55–8.47 (m, 3H, H^{A3} **and** H^{C2}), 8.19 (dt, J = 7.8, 1.7 Hz, 1H, H^{C3}), 7.98–7.91 (m, 2H, H^{A2}), 7.74–7.68 (m, 1H, H^{C4}). **^{13}C NMR (100 MHz, DMSO)** δ 158.16 (C^{A5}), 154.72 (C^{B1}), 151.29 (C^{B3}), 151.02 (C^{A1}/C^{C5}), 150.97 (C^{A1}/C^{C5}), 150.33 (C^{C1}), 142.61 (C^{A3}), 138.13 (C^{C3}), 129.23 (C^{A2}), 126.16 (C^{C4}), 126.14 (C^{A4}), 122.83 (C^{C2}), 121.18 (C^{B2}).

***2*: Yield 72%**. $C_{20}H_{14}ClN_4Pt$, CF_3O_3S. **Anal**. calcd: C 36.56% H 2.05% N 8.12% found: C 36.47%, H 2.22%, N 8.09%. **HRMS (ESI)**: calcd for $C_{20}H_{14}ClN_4Pt$ 540.0551 found 540.0555. **IR (KBr; cm^{-1})**: 3449 $\nu_{(OH)}$; 3075$\nu_{(ArH)}$; 1608 $\nu_{(C=N,\ C=C)}$; 1480, 1399 $d_{(C–CH\ out\ of\ the\ plane)}$; 1260 $\nu_{as(SO3)}$; 1154 $\nu_{(C–N)}$; 1097 $\delta_{(C–CH\ in\ the\ plane)}$; 1031 $\nu_{as(SO3)}$; 788 $\delta_{(C–C\ out\ of\ the\ plane)}$; 657 $\delta_{(C–C\ in\ the\ plane)}$; 638 $\delta_{(SO3)}$. **^1H NMR (400 MHz, DMSO)** δ 9.32 (s, 1H, H^{C6}), 8.92 (s, 2H, H^{B2}), 8.86 (d, J = 4.5 Hz, 1H, H^{C4}), 8.65 (d, J = 8.0 Hz, 2H, H^{A4}), 8.60 (d, J = 5.4 Hz, 2H, H^{A1}), 8.49 (d, J = 7.9 Hz, 1H, H^{C2}), 8.41 (t, J = 7.8 Hz, 2H, H^{A3}), 7.81 (t, J = 6.6 Hz, 2H, H^{A2}), 7.72 (dd, J = 7.3, 5.1 Hz, 1H, H^{C3}). **^{13}C NMR (100 MHz, DMSO)** δ 157.76 (C^{A5}), 154.32 (C^{B1}), 152.12 (C^{C4}), 151.16 (C^{A1}), 149.98 (C^{B3}), 148.63 (C^{C6}), 142.60 (C^{A3}), 135.24 (C^{C2}), 130.39 (C^{C1}), 129.34 (C^{A2}), 126.05 (C^{A4}), 124.22 (C^{C3}), 121.51 (C^{B2}).

***[PtCl(terpy)](SO$_3$CF$_3$)*: HRMS (ESI)**: calcd for $C_{15}H_{11}ClN_3Pt$ 463.0285 found 463.0292. **^1H NMR (400 MHz, DMSO)** δ 8.64 (d, J = 5.2 Hz, 2H, H^{A1}), 8.55–8.50 (m, 5H, $H^{A4,\ B2,\ B3}$), 8.44 (t, J = 7.7 Hz, 2H, H^{A3}), 7.85 (t, J = 6.4 Hz, 2H, H^{A2}). **^{13}C NMR (100 MHz, DMSO)** δ 158.14 (C^{A5}), 154.24 (C^{B1}), 151.06 (C^{A1}), 142.72 (C^{A3}), 142.12 (C^{B3}), 129.21 (C^{A2}), 125.86 (C^{A4}), 124.49 (C^{B2}).

Table 3
Crystal data and structure refinement.

	1	2
Empirical formula	$C_{20}H_{14}ClN_4Pt$, CF_3O_3S	$C_{20}H_{14}ClN_4Pt$, CF_3O_3S
Formula weight	689.96	689.96
Temperature [K]	295(2)	295(2)
Crystal system	Triclinic	Triclinic
Space group	$P\bar{1}$	$P\bar{1}$
Unit cell dimensions		
a [Å]	7.8189(3)	7.7706(5)
b [Å]	10.9006(4)	10.7776(12)
c [Å]	13.7527(5)	14.2210(11)
α [°]	106.388(3)	108.343(9)
β [°]	95.942(3)	92.338(6)
γ [°]	102.559(3)	106.528(8)
Volume [Å^3]	1080.47(7)	1072.59(17)
Z	2	2
Calculated density [Mg/m^3]	2.121	2.136
Absorption coefficient [mm^{-1}]	6.773	6.823
F(000)	2.121	660
Crystal dimensions [mm]	0.24 × 0.17 × 0.06	0.24 × 0.14 × 0.05
θ range for data collection [°]	3.25–29.37	3.34–29.48
Index ranges	$-10 \le h \le 10$, $-14 \le k \le 13$, $-18 \le l \le 18$	$-9 \le h \le 10$, $-14 \le k \le 14$, $-19 \le l \le 18$
Reflections collected	19,951	10,349
Independent reflections	5372 [R(int) = 0.0543, R_σ = 0.0553]	5097 [R(int) = 0.0664, R_σ = 0.0913]
Data/restraints/parameters	5372/0/307	5097/0/307
Goodness-of-fit on F^2	1.030	0.997
Final R indices [$I > 2\sigma(I)$]	R_1 = 0.0424, wR_2 = 0.1007	R_1 = 0.0657, wR_2 = 0.1386
R indices (all data)	R_1 = 0.0624, wR_2 = 0.0906	R_1 = 0.0954, wR_2 = 0.1563
Largest diff. peak and hole	1.341/−0.991	3.075/−2.629
CCDC number	1915296	1511103

4.3. Crystallography

The crystal of the compound was mounted in turn on a Gemini A Ultra Oxford Diffraction automatic diffractometer equipped with a CCD detector, and used for data collection. X-ray intensity data were collected with graphite monochromated MoK_α radiation (λ = 0.71073 Å) at a temperature of 295(2) K, with ω scan mode. Ewald sphere reflections were collected up to $2\theta = 50.10^\circ$. Details concerning crystal data and refinement are gathered in Table 3. Lorentz, polarization and empirical absorption corrections using spherical harmonics implemented in SCALE3 ABSPACK scaling algorithm [113] were applied. The structures were solved by the Patterson method and subsequently completed by difference Fourier recycling. All the non-hydrogen atoms were refined anisotropically using full-matrix, least-squares techniques. All hydrogen atoms were positioned in geometrically idealized positions and were allowed to ride on their parent atoms with $U_{iso}(H) = 1.2\ Ueq$. The Olex2 [114] and SHELXS, SHELXL [115] programs were used for all the calculations. Atomic scattering factors were incorporated in the computer programs.

4.4. Biological studies

4.4.1. Cell lines

All used cell lines (malignant melanoma Me45, adenocarcinomic human alveolar basal epithelial cells A549, human breast adenocarcinoma MCF-7, cervical cancer HeLa, normal human dermal fibroblasts NHDF, human bronchial epithelial cell line BEAS-2B, normal human fibroblasts GM07492) came from the collection obtained from the Center for Translation and Molecular Biology of Cancers of the Institute of Oncology in Gliwice. The human colorectal carcinoma cell line (HCT116) and its variant with knock-out of p53 gene (HCT116p53-/-), were obtained courtesy of Prof. Marek Rusin. The cells were grown in Dulbecco's Modified Eagle Medium/Nutrient Mixture F-12 (DMEM F12, Sigma-Aldrich) which is a widely used basal medium for supporting the growth of many kinds of mammalian cells. Tumor cell lines were cultured, supplementing the medium with 12% heat-activated fetal bovine serum (FBS, EURx), while the normal lines were cultured with 15% non-inactivated serum. The Penicillin-Streptomycin (100x, Sigma-Aldrich) was used in recommended for application concentration, to protect cell culture from bacterial contamination. All cells were grown as monolayer cultures in 75 cm^2 bottles (Nest Scientific Biotechnology) and maintained in constant 80% humidity atmospheres and 5% carbon dioxide concentration at 37 °C (Heracell™ 150i, from Thermo Scientific™). The cells were obtained by trypsynisation with a 0.25% trypsin-EDTA (Sigma-Aldrich). Trypsin was neutralized by the addition of an equal amount of culture medium. After centrifugation (1500 rpm for 5 min) and deprivation in fresh medium, the cells were counted with Automatic Cell Counter T^{10} (Bio-Rad).

4.4.2. The cytotoxicity by the MTS assay

The cytotoxicity of the compounds was determined by the colorimetric method described in detail in the previous publication [42]. In this assay, the amount of colored reaction product is proportional to the number of viable cells. Cells in the exponential growth phase were seeded into a 96-well plate (NEST Scientific) in 200 µl of complete medium. Cells were seeded per each well in an amount of: 4 × 10^3 cells for HCT116, HCT116p53-/-, HeLa, NHDF and GM 07492, 3 × 10^3 cells for MCF-7 and BEAS-2B, 2 × 10^3 cells for Me45 and 1.5 × 10^3 cells for A549. Approximately 24 h after seeding the cells, the compounds were dissolved in sterile DMSO (Sigma-Aldrich) and then diluted with culture medium to obtain final concentrations of 0.01 µM ÷ 100 µM and not exceed the final concentration of 0.3% DMSO. For comparison purpose, the studies were also performed for Cisplatin, which was prepared according to the product protocol. After 72 h, the solution of the compound was removed, the plate was rinsed with PBS and 100 µl of DMEM medium (Sigma-Aldrich) without phenol red was added to each well. The MTS test was then performed according to the protocol of the CellTiter 96® AQueous One Solution Cell Proliferation Assay (Promega). After 30 min of incubation of cells, the absorbance was measured using a SYNERGY4 multi-well plate reader (BioTek Instruments, USA). The number of viable cells was determined with reference to control cells, not treated with any agent and growing under standard conditions.

4.4.3. F-actin visualization/cell morphology assessment

A549 cells were seeded in glass bottom µ-dish (Ibidi, GmbH) at a density of 15,000 cells per 35-mm dish in 1 ml of complete medium and allowed to attach for 24 h. The cells were then treated with **2** (2,5 µM solution in medium) for 3, 6, 24, 48 or 72 h. When the treatment was completed, the cells were rinsed 3 times with pre-warmed PBS without Ca^{2+} and Mg^{2+} and fixed in 3.7% formaldehyde for 10 min. After rinsing with PBS the cells were permeabilized for 4 min with 0.1% Triton X-100 in PBS and blocked for 30 min in 1% (*w/v*) BSA (bovine serum albumin). Next, cells were incubated with 170 nM Alexa Fluor 488 phalloidin (Invitrogen™) for 30 min at room temperature and then then rinsed three times with PBS. DNA was counterstained with Hoechst 33342 (1 µg/ml in PBS, Invitrogen™) for 5 min. After extensive washing the samples were mounted in Fluoromount (Sigma-Aldrich) and imaged on Zeiss LSM 780 confocal microscope with Airyscan under 63× or 40× objectives. 405 nm and 488 nm laser wavelengths were used to excite Hoechst and AlexaFluor 488 respectively.

4.4.4. Cell cycle

The A549 cells were seeded at 10^4 cells per well in 4 ml of complete medium for 6 wells culture plates. After about 24 h cells were treated with the compound at a concentration equal to the IC_{50} dose for a further 1, 3, 6, 12, 24, 48, 72 and 96 h. Next, cells were harvested by trypsinization, pelleted by centrifugation at 1300 rpm for 5 min (including cells from old medium), washed three times with sterile PBS buffer and centrifuged again under the same conditions. Subsequently, 0.5 ml of ice-cold 70% ethanol was added to the cells by slowly dropping and gentle shaking. Such fixed cells were stored at −20 °C until analysis. Before measurement, the cells were centrifuged (1300 rpm, 3 min), rinsed with sterile PBS buffer and centrifuged again. Then, the supernatant was removed and the cells resuspended in 50 µl PBS and 50 µl RNAse (100 µg/ml). After 15 min of incubation, the cells were stained with propidium iodide (100 µg/ml, Sigma-Aldrich) holding them in the dark for a further 15 min, and finally, the samples were analyzed using a flow cytometer (Aria III, Becton Dickinson UK). Fluorescence was measured using a flow cytometer with the PE configuration (547 nm excitation laser line; emission: 585 nm). At least 10,000 cells were analyzed for each sample, recording the DNA content as a differentiating parameter.

4.4.5. Apoptosis analysis

The number of necrotic and apoptotic cells was also counted using the FITC Annexin V Apoptosis Detection Kit with PI (Bio Legend). Cells collected at different times were rinsed twice and finally resuspended in 50 µl of Annexin V Binding Buffer, 2.5 µl of FITC Annexin V and 10 µl propidium iodide (100 µg/ml). Next the samples were vortexed gently and incubated for 15 min at room temperature (25 °C) in the dark. Before measurement 250 µl of Annexin V Binding Buffer was added to each tube. The fluorescence of PI (necrotic cells) was detected at configuration for PE channel, and for Annexin V FITC-conjugated antibody (apoptotic cells) at FITC channel configuration (488 nm excitation laser line; emission: LP mirror 503, BP filter 530/30).

4.4.6. Mitotic index determination

The samples were prepared similarly as in case of F-actin visualization with the omission of permeabilization, blocking and incubation in fluorescent phalloidin and subsequently observed under Zeiss Z1 AxioObserver epifluorescence microscope. Images were captured with camera AxioCam MRm and Carl Zeiss™ AxioVision Rel. 4.8.2 software. At least 1000 cells per treatment were scored for the presence of mitotic figures and micronuclei. Mitotic index (and phase indices) were calculated as the ratio between the number of cells undergoing division (or in a specific phase of the division) to the total number of cells. Statistical analysis was performed using the chi-square test.

4.4.7. Analysis of the level of reactive oxygen species

The level of intracellular reactive oxygen species (ROS) was determined using 2′,7′-dichlorodihydrofluorescein diacetate (DCFH-DA) (Sigma-Aldrich) and flow cytometry. DCFH-DA diffuses through cell membranes and then is converted by intracellular esterases into 2′,7′-dichlorodihydrofluorescein (DCFH). This one in turn, oxidized in the cytosol by free radicals, becomes a fluorescent compound 2′,7′-dichlorofluorescein (DCF) and thus a sensitive marker of oxidative stress. The level of intracellular reactive oxygen species was determined from the part of A549 cells incubated with the compound at IC_{50} concentration and harvested at 1, 3, 6, 12, 24, 48, 72 and 96 h. Next the cells were resuspended in 300 µl of culture medium and 10 µl 2′,7′-dichlorofluorescin diacetate (30 µM; Sigma-Aldrich, cat. No292648) and incubated in the dark for 30 min and 37 °C. After the required time the cells were centrifuged for 3 min, at 4 °C and 2500 rpm, washed, resuspended in 300 µl of PBS and kept for 15 min on ice under dark conditions. The samples prepared for measurement were stored on ice and finally analyzed using a flow cytometer (Aria III, Becton Dickinson UK). At least 10,000 cells were analyzed for each sample. Fluorescence was measured using a flow cytometer with the FITC configuration (488 nm excitation laser line; emission: LP mirror 503, BP filter 530/30).

4.4.8. The mass of mitochondria and the mitochondrial potential $\Delta\Psi_m$

Mass of mitochondria and mitochondrial potential was determined from the pool of cells incubated with the compound **2** at IC_{50} concentration and then harvested in appropriate times. The mass of mitochondria in cells was evaluated using the fluorescent dye 3,6-*bis*(dimethylamino)-10-nonyl-acridinium bromide (NAO, Invitrogen™) that binds to the mitochondria. Each sample (300 µl) was incubated for 20 min at 37 °C with 100 nM NAO solution. In order to determine the change in mitochondrial potential $\Delta\Psi_m$, the tetramethylrhodamine ethyl ester perchlorate (TMRE, Sigma-Aldrich) specifically bind to the inner side of the mitochondrial membrane was used. Cells (300 µl) were incubated for 20 min at 37 °C with 50 nM TMRE solutions. The samples were then centrifuged, resuspended in PBS and analyzed by flow cytometer. Fluorescence for mitochondrial potential was measured using a flow cytometer with the PE configuration (547 nm excitation laser line; emission: 585 nm). Configuration for mitochondrial mass was set as for the FITC channel (488 nm excitation laser line; emission: LP mirror 503, BP filter 530/30), respectively.

4.4.9. RNA isolation

The RNA isolation was performed using GeneMATRIX Universal RNA Purification Kit (EURx) following the manufacturer's protocol, from samples collected at a different time points (3, 6, 24, 48 or 72 h) from cells incubated with IC_{50} dose of tested compound. RNA was quantified by absorbance, measurement at 260 nm using a NanoDrop 2000 spectrophotometer (Thermo Scientific), where quality and amount of isolated RNA were specified.

4.4.10. Reverse transcription

The A549 cells were incubated with the compound **2** at a concentration equal to the IC_{50} or with DMEM F12 (control) for a different time: 12, 24, 48 and 72 h. In the next step, cells were trypsinized, washed with PBS and stored at −20 °C until RNA isolation. Equal amount of obtained total RNA from each sample was reverse-transcribed into cDNA using NG dART RT kit (EURx) and C1000 Touch Thermal Cycler (Bio-Rad), within producer protocol. Obtained cDNA were stored at −20 °C. Prior real time PCR reaction adequate samples of cDNA solutions were prepared using RNase free water (EURx).

4.4.11. Quantitative real time polymerase chain reaction (qRT-PCR)

The qPCR was performed using SG qPCR Master Mix (EURx) according to the producer protocol. 5 µg of total RNA was used for cDNA synthesis (25 µl total volumes). ct-DNA was diluted 100-fold and 6-µl aliquots were used for Real-Time PCR performed on CFX96 Real-Time System (Bio-Rad) within reaction profile: 4 min at 95 °C; 54 cycles of 30 s at 95 °C; 30 s at 56 °C; and 30 s at 72 °C; final melting curve at 52–92 °C (every 0.5 °C at 5 s). Set of primers (Genomed; Poland) for IL-6 and IL-8 amplification, and genes from DNA damage and repair pathway: ERCC3 (NER; Nucleotide Excision Repair), OGG1 (BER; Base Excision Repair) and XRCC4 (NHEJ; Non-Homologous End Joining) were chosen (2 pM per each reaction/well). For genes expression normalisation reference gen of RPL41 from ribosomal subunit was used. Sequences of set of primers: IL-6 reverse: 5′-AGATCACCTAGTCCACC CCC-3′; IL-6 forward: 5′-GTTCTGCCAAACCAGCCTTG-3′; IL-8 reverse: 5′-ACCAAGGCACAGTGGAACAA-3′; IL-8 forward: 5′-GGTGCAGTTTTG CCAAGGAG-3′; ERCC3 (NER) reverse: 5′-CTTGTCCTTGGCATCGG AGG-3′; ERCC3 (NER) forward: 5′-GCTGGAAAGTCCCTGGTTGG-3′; BER (OGG1) reverse: 5′-CCTGACAGCACCGCTTGG-3′; BER (OGG1) forward: 5′-CTGCATCCTGCCTGGAGTGG-3′; NHEJ (XRCC4) reverse: 5′-CCCAGTCCATGCTGAATGACC-3′; NHEJ (XRCC4) forward: 5′-CGGA AGTAGAGTCACGGAGAGG-3′; RAD51 (HR) reverse: 5′-CACACATCCA AATGCCAGTGC-3′; RAD51 (HR) forward: 5′-GAAGTGGAGCGTAAGC

CAG-3′; RPL41 (reference) reverse: 5′-ACGGTGCAACAAGCTAGCGG-3′; RPL41 (reference) forward: 5′-TCCTGCGTTGGGATTCCGTG-3′.

The calculation of standardized value of relative gene expression level in an unknown sample, in relation to control, is performed in accordance with the formula $R = 2^{-\Delta\Delta Ct}$ and results presented as log2 (where, value 0 means any changes in gene expression; −1 down-regulation; +1 up-regulation) [116]. Results obtained from three independent experiments in triplicate, and presented as mean ± SD.

Abbreviations

^{3}MC	triplet metal-centered excited state
4′-R^1-terpy	4′-(2-pyridyl)-2,2′:6′,2″-terpyridine
4′-R^2-terpy	4′-(3-pyridyl)-2,2′:6′,2″-terpyridine
9-EtG	9-ethylguanine
A549	non-small lung adenocarcinoma cells
BEAS-2B	human bronchial epithelial cells
BER	Base Excision Repair
BSA	bovine serum albumin
CDKs	cycline-dependent kinases
COSY	2D NMR correlation spectroscopy
ct-DNA	calf thymus DNA
CV	cyclic voltammetry
DCF	2′,7′-dichlorofluorescein
DCFH	2′,7′-dichlorodihydrofluorescein
DCFH-DA	2′,7′-dichlorodihydrofluorescein diacetate
DMEM	Dulbecco's Modified Eagle Medium/Nutrient Mixture F-12
DMSO	dimethyl sulfoxide
DPV	differential pulse voltammetry
EB	ethidium bromide
ESI-HRMS	high resolution electrospray ionization mass spectroscopy
FITC	fluorescein isothiocyanate
FT-IR	Fourier transformed infrared spectroscopy
GM07492	normal human fibroblast cells
HCT116	human colon cancer cell line
HCT116p53-/-	human colon cancer cell line with p53 gene silenced
HeLa	human cervical cancer cell line
HMBC	heteronuclear multiple bond correlation 2D NMR spectroscopy
HMQC	heteronuclear multiple quantum correlation 2D NMR spectroscopy
HR	Homologous Recombination
IC_{50}	half-minimal inhibitory concentration
IL	intraligand transitions
IL-6	interleukin 6
IL-8	interleukin 8
IRF	instrument response function
MCF-7	breast cancer cells
Me45	malignant melanoma cell line
MLCT	metal-to-ligand charge transfer transitions
MTS	3-(4,5-dimethylthiazol-2-yl)-5-(3-carboxymethoxyphenyl)-2-(4-sulfophenyl)-2H-tetrazolium
NER	Nucleotide Excision Repair
NHDF	Normal Human Dermal Fibroblasts
NHEJ	Non-Homologous End Joining
NMR	nuclear magnetic resonance spectroscopy
PBS	phosphate buffered saline
PI	propidium iodide
qRT-PCR	quantitative real time polymerase chain reaction
Q-TOF	quadrupole time-of-flight mass spectrometry analyzer
ROS	reactive oxygen species
SD	standard deviation
SI	selectivity index
TCSPC	time-correlated single photon counting
Terpy	2,2′:6′,2″-terpyridine
UV–Vis	ultraviolet–visible spectroscopy

Acknowledgements

This research did not receive any specific grant from funding agencies in the public, commercial, or not-for-profit sectors.

Declaration of competing interest

None.

Appendix A. Supplementary data

Supplementary data to this article can be found online at https://doi.org/10.1016/j.jinorgbio.2019.110809.

References

[1] W. Goodall, J.A.G. Williams, Chem. Commun. 0 (2001) 2514–2515.
[2] W. Goodall, K. Wild, K.J. Arm, J.A.G. Williams, J. Chem. Soc. Perkin Trans. 2 (0) (2002) 1669–1681.
[3] R. Siebert, A. Winter, U.S. Schubert, B. Dietzek, J. Popp, J. Phys. Chem. C 114 (2010) 6841–6848.
[4] A. Wild, A. Winter, F. Schlütter, U.S. Schubert, Chem. Soc. Rev. 40 (2011) 1459–1511.
[5] J. Husson, M. Knorr, J. Heterocyclic Chem. 49 (2012) 453–478.
[6] Q.-Y. Cao, M. Li, L. Zhou, Z.-W. Wang, RSC Adv. 4 (2013) 4041–4046.
[7] S. Wang, F. Zhao, S. Luo, Y. Geng, Q. Zeng, C. Wang, Phys. Chem. Chem. Phys. 17 (2015) 12350–12355.
[8] P. Shi, Q. Jiang, X. Zhao, Q. Zhang, Y. Tian, Dalton Trans. 44 (2015) 8041–8048.
[9] B.N. Ghosh, F. Topić, P.K. Sahoo, P. Mal, J. Linnera, E. Kalenius, H.M. Tuononen, K. Rissanen, Dalton Trans. 44 (2014) 254–267.
[10] S.-Y. Jiao, K. Li, W. Zhang, Y.-H. Liu, Z. Huang, X.-Q. Yu, Dalton Trans. 44 (2014) 1358–1365.
[11] A. Maroń, A. Szlapa, T. Klemens, S. Kula, B. Machura, S. Krompiec, J.G. Małecki, A. Świtlicka-Olszewska, K. Erfurt, A. Chrobok, Org. Biomol. Chem. 14 (2016) 3793–3808.
[12] H. Sasabe, Y. Hayasaka, R. Komatsu, K. Nakao, J. Kido, Chem. Eur. J. 23 (2017) 114–119.
[13] H. Yamazaki, T. Ueno, K. Aiso, M. Hirahara, T. Aoki, T. Nagata, S. Igarashi, M. Yagi, Polyhedron 52 (2013) 455–460.
[14] C. Zhang, P. Srivastava, K. Ellis-Guardiola, J.C. Lewis, Tetrahedron 70 (2014) 4245–4249.
[15] E.K. Beloglazkina, A.G. Majouga, E.A. Manzheliy, A.A. Moiseeva, Y.V. Lin'kova, N.V. Zyk, Polyhedron 85 (2015) 800–808.
[16] L. Li, Y.Z. Zhang, C. Yang, E. Liu, J.A. Golen, G. Zhang, Polyhedron 105 (2016) 115–122.
[17] V. Duprez, M. Biancardo, H. Spanggaard, F.C. Krebs, Macromolecules 38 (2005) 10436–10448.
[18] I. Eryazici, C.N. Moorefield, G.R. Newkome, Chem. Rev. 108 (2008) 1834–1895.
[19] R. Siebert, A. Winter, B. Dietzek, U.S. Schubert, J. Popp, Macromol. Rapid Commun. 31 (2010) 883–888.
[20] A. Winter, M.D. Hager, G.R. Newkome, U.S. Schubert, Adv. Mater. 23 (2011) 5728–5748.
[21] N.S. Murray, S. Keller, E.C. Constable, C.E. Housecroft, M. Neuburger, A. Prescimone, Dalton Trans. 44 (2015) 7626–7633.
[22] H. Hofmeier, U.S. Schubert, Chem. Soc. Rev. 33 (2004) 373–399.
[23] E.C. Constable, G. Zhang, C.E. Housecroft, M. Neuburger, J.A. Zampese, CrystEngComm 12 (2010) 3733–3739.
[24] E.C. Constable, C.E. Housecroft, M. Neuburger, S. Vujovic, J.A. Zampese, G. Zhang, CrystEngComm 14 (2012) 3554–3563.
[25] Y.M. Klein, A. Prescimone, E.C. Constable, C.E. Housecroft, CrystEngComm 17 (2015) 6483–6492.
[26] H. Bertrand, D. Monchaud, A.D. Cian, R. Guillot, J.-L. Mergny, M.-P. Teulade-Fichou, Org. Biomol. Chem. 5 (2007) 2555–2559.
[27] S.D. Cummings, Coord. Chem. Rev. 253 (2009) 1495–1516.
[28] D. Mahendiran, P. Gurumoorthy, K. Gunasekaran, R.S. Kumar, A.K. Rahiman, New J. Chem. 39 (2015) 7895–7911.
[29] V.S. Stafford, K. Suntharalingam, A. Shivalingam, A.J.P. White, D.J. Mann, R. Vilar, Dalton Trans. 44 (2015) 3686–3700.
[30] D. Mahendiran, R.S. Kumar, V. Viswanathan, D. Velmurugan, A.K. Rahiman, Dalton Trans. 45 (2016) 7794–7814.
[31] D. Mahendiran, R.S. Kumar, A.K. Rahiman, Mater. Sci. Eng. C 76 (2017) 601–615.
[32] W. Leslie, A.S. Batsanov, J.A.K. Howard, J.A.G. Williams, Dalton Trans. 0 (2004) 623–631.
[33] J.A.G. Williams, A.J. Wilkinson, V.L. Whittle, Dalton Trans. 0 (2008) 2081–2099.
[34] S. Muratsugu, H. Nishihara, New J. Chem. 38 (2014) 6114–6124.
[35] M. Humbert-Droz, C. Piguet, T.A. Wesolowski, Phys. Chem. Chem. Phys. 18 (2016) 29387–29394.
[36] D. Jaganyi, A. Hofmann, R. van Eldik, Angew. Chem. Int. Ed. Eng. 40 (2001) 1680–1683.
[37] A. Hofmann, D. Jaganyi, O.Q. Munro, G. Liehr, R. van Eldik, Inorg. Chem. 42 (2003) 1688–1700.

[38] D. Jaganyi, D. Reddy, J.A. Gertenbach, A. Hofmann, R. van Eldik, Dalton Trans. 0 (2004) 299–304.
[39] N. Summa, W. Schiessl, R. Puchta, N. van Eikema Hommes, R. van Eldik, Inorg. Chem. 45 (2006) 2948–2959.
[40] M.-Y. Ho, M.-L. Chiou, W.-S. Du, F.Y. Chang, Y.-H. Chen, Y.-J. Weng, C.-C. Cheng, J. Inorg. Biochem. 105 (2011) 902–910.
[41] B.B. Khusi, A. Mambanda, D. Jaganyi, Transit. Met. Chem. 41 (2016) 191–203.
[42] K. Czerwińska, M. Golec, M. Skonieczna, J. Palion-Gazda, D. Zygadło, A. Szlapa-Kula, S. Krompiec, B. Machura, A. Szurko, Dalton Trans. 46 (2017) 3381–3392.
[43] L. Hou, D. Li, W.-J. Shi, Y.-G. Yin, S.W. Ng, Inorg. Chem. 44 (2005) 7825–7832.
[44] L. Gou, Q.-R. Wu, H.-M. Hu, T. Qin, G.-L. Xue, M.-L. Yang, Z.-X. Tang, Polyhedron 27 (2008) 1517–1526.
[45] L. Gou, B. Zhang, H.-M. Hu, X.-L. Chen, B.-C. Wang, Q.-R. Wu, T. Qin, Z.-X. Tang, J. Mol. Struct. 889 (2008) 244–250.
[46] J.E. Beves, E.C. Constable, S. Decurtins, E.L. Dunphy, C.E. Housecroft, T.D. Keene, M. Neuburger, S. Schaffner, J.A. Zampese, CrystEngComm 11 (2009) 2406–2416.
[47] M. Liang, J. Chen, Chem. Soc. Rev. 42 (2013) 3453–3488.
[48] S.C. Dhara, Indian J. Chem. 8 (1970) 193–194.
[49] G.A. Lawrance, Chem. Rev. 86 (1986) 17–33.
[50] L. Yang, D.R. Powell, R.P. Houser, Dalton Trans. 0 (2007) 955–964.
[51] A. Okuniewski, D. Rosiak, J. Chojnacki, B. Becker, Polyhedron 90 (2015) 47–57.
[52] R. Büchner, C.T. Cunningham, J.S. Field, R.J. Haines, D.R. McMillin, G.C. Summerton, J. Chem. Soc. Dalton Trans. 0 (1999) 711–718.
[53] H.-K. Yip, L.-K. Cheng, K.-K. Cheung, C.-M. Che, J. Chem. Soc. Dalton Trans. 0 (1993) 2933–2938.
[54] A. Maroń, A. Szlapa, K. Czerwińska, J.G. Małecki, S. Krompiec, B. Machura, CrystEngComm 18 (2016) 5528–5536.
[55] J. Huo, N. Arulsamy, J.O. Hoberg, Dalton Trans. 40 (2011) 7534–7540.
[56] J.S. Field, C.R. Wilson, O.Q. Munro, Inorg. Chim. Acta 374 (2011) 197–204.
[57] A. Maroń, K. Czerwińska, B. Machura, L. Raposo, C. Roma-Rodrigues, A.R. Fernandes, J.G. Małecki, A. Szlapa-Kula, S. Kula, S. Krompiec, Dalton Trans. 47 (2018) 6444–6463.
[58] H.-H. Zou, L. Wang, Z.-X. Long, Q.-P. Qin, Z.-K. Song, T. Xie, S.-H. Zhang, Y.-C. Liu, B. Lin, Z.-F. Chen, Eur. J. Med. Chem. 108 (2016) 1–12.
[59] E. Sakuda, A. Funahashi, N. Kitamura, Inorg. Chem. 45 (2006) 10670–10677.
[60] T. Yutaka, I. Mori, M. Kurihara, J. Mizutani, N. Tamai, T. Kawai, M. Irie, H. Nishihara, Inorg. Chem. 41 (2002) 7143–7150.
[61] T.J. Wadas, Q.-M. Wang, Y. Kim, C. Flaschenreim, T.N. Blanton, R. Eisenberg, J. Am. Chem. Soc. 126 (2004) 16841–16849.
[62] A. Han, P. Du, Z. Sun, H. Wu, H. Jia, R. Zhang, Z. Liang, R. Cao, R. Eisenberg, Inorg. Chem. 53 (2014) 3338–3344.
[63] G. Zhang, Q. Li, W. Fu, D. Wang, Acta Crystallogr., Sect. E: Struct. Rep. Online 66 (2010) m681.
[64] J.S. Field, J.-A. Gertenbach, R.J. Haines, L.P. Ledwaba, N.T. Mashapa, D.R. McMillin, O.Q. Munro, G.C. Summerton, Dalton Trans. 0 (2003) 1176–1180.
[65] J.S. Field, R.J. Haines, D.R. McMillin, G.C. Summerton, J. Chem. Soc. Dalton Trans. 0 (2002) 1369–1376.
[66] A. Maroń, K. Czerwińska, J.G. Małecki, B. Machura, A. Szłapa-Kula, S. Krompiec, ChemistrySelect 2 (2017) 1071–1078.
[67] D.P. Lazzaro, P.E. Fanwick, D.R. McMillin, Inorg. Chem. 51 (2012) 10474–10476.
[68] M.A. Spackman, J.J. McKinnon, CrystEngComm 4 (2002) 378–392.
[69] M.A. Spackman, D. Jayatilaka, CrystEngComm 11 (2009) 19–32.
[70] S.K. Wolff, D.J. Grimwood, J.J. McKinnon, M.J. Turner, D. Jayatilaka, M.A. Spackman, Crystal Explorer, University of Western Australia, 2012.
[71] M.H. Wilson, L.P. Ledwaba, J.S. Field, D.R. McMillin, Dalton Trans. 0 (2005) 2754–2759.
[72] M.G. Hill, J.A. Bailey, V.M. Miskowski, H.B. Gray, Inorg. Chem. 35 (1996) 4585–4590.
[73] Q.-Z. Yang, L.-Z. Wu, Z.-X. Wu, L.-P. Zhang, C.-H. Tung, Inorg. Chem. 41 (2002) 5653–5655.
[74] V.W.-W. Yam, R.P.-L. Tang, K.M.-C. Wong, K.-K. Cheung, Organometallics 20 (2001) 4476–4482.
[75] X. Liu, E.J.L. McInnes, C.A. Kilner, M. Thornton-Pett, M.A. Halcrow, Polyhedron 20 (2001) 2889–2900.
[76] D.K. Crites, C.T. Cunningham, D.R. McMillin, Inorg. Chim. Acta 273 (1998) 346–353.
[77] J.F. Michalec, S.A. Bejune, D.G. Cuttell, G.C. Summerton, J.A. Gertenbach, J.S. Field, R.J. Haines, D.R. McMillin, Inorg. Chem. 40 (2001) 2193–2200.
[78] R.D. Rakhimov, Yu.A. Weinstein, E.V. Lileeva, N.N. Zheligovskaya, M.Ya. Mel'nikov, K.P. Butin, Russ. Chem. Bull. 52 (2003) 1150–1156.
[79] E.M.A. Ratilla, H.M. Brothers, N.M. Kostic, J. Am. Chem. Soc. 109 (1987) 4592–4599.
[80] D.R. McMillin, J.J. Moore, Coord. Chem. Rev. 229 (2002) 113–121.
[81] J.F. Michalec, S.A. Bejune, D.R. McMillin, Inorg. Chem. 39 (2000) 2708–2709.
[82] J.H. Blanch, J. Chem. Soc. B 0 (1966) 937–939.
[83] P. Nikolov, F. Fratev, O.E. Polansky, J. Mol. Struct. 114 (1984) 265–268.
[84] K.W. Jennette, J.T. Gill, J.A. Sadownick, S.J. Lippard, J. Am. Chem. Soc. 98 (1976) 6159–6168.
[85] J.A. Bailey, M.G. Hill, R.E. Marsh, V.M. Miskowski, W.P. Schaefer, H.B. Gray, Inorg. Chem. 34 (1995) 4591–4599.
[86] M. Casamento, G.E. Arena, C. Lo Passo, I. Pernice, A. Romeo, L.M. Scolaro, Inorg. Chim. Acta 275–276 (1998) 242–249.
[87] G. Arena, L.M. Scolaro, R.F. Pasternack, R. Romeo, Inorg. Chem. 34 (1995) 2994–3002.
[88] G. Annibale, M. Brandolisio, Z. Bugarcic, L. Cattalini, Transit. Met. Chem. 23 (1998) 715–719.
[89] B.V. Petrovic, M.I. Djuran, Z.D. Bugarcic, Metal-Based Drugs 6 (1999) 355–360.
[90] R. Büchner, J.S. Field, R.J. Haines, C.T. Cunningham, D.R. McMillin, Inorg. Chem. 36 (1997) 3952–3956.
[91] D.-L. Ma, T.Y.-T. Shum, F. Zhang, C.-M. Che, M. Yang, Chem. Commun. 0 (2005) 4675–4677.
[92] W.D. McFadyen, L.P. Wakelin, I. a. G. Roos, B.L. Hillcoat, Biochem. J. 242 (1987) 177–183.
[93] M.L. Clark, R.L. Green, O.E. Johnson, P.E. Fanwick, D.R. McMillin, Inorg. Chem. 47 (2008) 9410–9418.
[94] A. McCoubrey, H.C. Latham, P.R. Cook, A. Rodger, G. Lowe, FEBS Lett. 380 (1996) 73–78.
[95] M. Howe-Grant, K.C. Wu, W.R. Bauer, S.J. Lippard, Biochemistry 15 (1976) 4339–4346.
[96] S.W.A. Bligh, A. Bashall, C. Garrud, M. McPartlin, N. Wardle, K. White, S. Padhye, V. Barve, G. Kundu, Dalton Trans. 0 (2003) 184–188.
[97] J.A. Todd, L.M. Rendina, Inorg. Chem. 41 (2002) 3331–3333.
[98] G. Scatchard, Ann. N. Y. Acad. Sci. 51 (1949) 660–672.
[99] J.-B. Lepecq, C. Paoletti, J. Mol. Biol. 27 (1967) 87–106.
[100] O. Stern, M. Volmer, Phys. Z. (1919) 183–188.
[101] A. Wolfe, G.H. Shimer, T. Meehan, Biochemistry 26 (1987) 6392–6396.
[102] J.R. Lakowicz, G. Weber, Biochemistry 12 (1973) 4161–4170.
[103] M. Lee, A.L. Rhodes, M.D. Wyatt, S. Forrow, J.A. Hartley, Biochemistry 32 (1993) 4237–4245.
[104] A. Mogilner, K. Keren, Curr. Biol. 19 (2009) R762–R771.
[105] L. Blanchoin, R. Boujemaa-Paterski, C. Sykes, J. Plastino, Physiol. Rev. 94 (2014) 235–263.
[106] H. Stopper, S.O. Müller, Toxicol. in Vitro 11 (1997) 661–667.
[107] L. Luzhna, P. Kathiria, O. Kovalchuk, Front. Genet. 4 (2013).
[108] J. Wang, G.S. Hanan, Synlett (2005) (2005) 1251–1254.
[109] A.N. Kharat, A. Bakhoda, S. Zamanian, Polyhedron 30 (2011) 1134–1142.
[110] E.C. Constable, E.L. Dunphy, C.E. Housecroft, M. Neuburger, S. Schaffner, F. Schaper, S.R. Batten, Dalton Trans. 0 (2007) 4323–4332.
[111] M.E. Reichmann, S.A. Rice, C.A. Thomas, P. Doty, J. Am. Chem. Soc. 76 (1954) 3047–3053.
[112] J. Marmur, J. Mol. Biol. 3 (1961) 208–IN1.
[113] CrysAlis PRO, Oxford Diffraction Ltd, Yarnton, England, 2011.
[114] O.V. Dolomanov, L.J. Bourhis, R.J. Gildea, J.A.K. Howard, H. Puschmann, J. Appl. Crystallogr. 42 (2009) 339–341.
[115] G.M. Sheldrick, Acta Crystallogr. C 71 (2015) 3–8.
[116] K.J. Livak, T.D. Schmittgen, Methods 25 (2001) 402–408.